Marine and Petroleum Geology 122 (2020) 104703

Contents lists available at ScienceDirect

Marine and Petroleum Geology

journal homepage: www.elsevier.com/locate/marpetgeo

Research paper

Fracture characterization in Upper Permian carbonates in Spitsbergen: A workflow from digital outcrop to geo-model

Kristine Larssen [a,b,c,*], Kim Senger [b], Sten-Andreas Grundvåg [c]

[a] Equinor ASA, Margrethe Jørgensens vei 13, 9406, Harstad, Norway
[b] Department of Arctic Geology, University Centre in Svalbard, P.O. Box 156, NO–9171, Longyearbyen, Norway
[c] Department of Geosciences, University of Tromsø—The Arctic University of Norway, P.O. Box 6050 Langnes, NO–9037, Tromsø, Norway

ARTICLE INFO

Keywords:
Svalbard
Workflow
Digital outcrop
Arctic
Carbonates
Geomodelling
Fractures
Discrete fracture modelling

ABSTRACT

Carbonates represent major hydrocarbon reservoirs, but often exhibit highly heterogeneous reservoir properties. Outcrop analogues provide important insights into how parameters such as porosity, permeability and natural fractures vary. As such, outcrops can bridge the scale gap between spatially extensive but poor-resolution seismic data and 1D high-resolution well data. However, traditional geological fieldwork typically gathers insufficient data to construct robust geological models. In this study, we have specifically set out to gather key data sets that enable the construction of a geology-driven model. We illustrate this workflow using the exceptionally well-exposed carbonate-dominated outcrops of the Kapp Starostin Formation in central Spitsbergen, Arctic Norway. We fully utilize emerging technologies, notably geo-referenced digital outcrop models (DOMs), to be able to gather quantitative sedimentological-structural data from otherwise inaccessible cliffs. DOMs generated from digital photos are used directly for automatic and manual mapping of fractures. The digital data are complemented with traditional fieldwork (sedimentological logging, scanlines, structural characterization) in order to strengthen the dataset. The geo-modelling involves traditional facies and petrophysical modelling of the 12 identified facies, along with outcrop-based discrete fracture modelling. Finally, the static geo-model is upscaled, and its applications are discussed. The presented workflow uses carbonate outcrops of the Kapp Starostin Formation as input but is highly applicable for other studies where outcrops can be utilized as direct input to constrain a geological model.

1. Introduction

Carbonate reservoirs represent important hydrocarbon reservoirs (Kingston et al., 1983; Roehl and Choquette, 2012), major groundwater aquifers (Lattman and Parizek, 1964), geothermal reservoirs (Montanari et al., 2017) and potential CO_2 sequestration sites (Shakiba et al., 2016). In contrast to most siliciclastic reservoirs, carbonates often exhibit heterogeneous reservoir properties. Porosity and permeability are controlled by processes at the time of carbonate growth, but also through burial diagenesis, post-depositional dissolution, and tectonic events (e.g., Bjorlykke, 1984). Pore systems in carbonate systems are thus often complex and span from the micro-scale (e.g. pores and fractures) to km-scale cave systems (Ahr, 2011; Loucks, 1999; Lønøy, 2006). Fracture systems, in particular, are important elements that contribute to improved reservoir properties and flow in many carbonate reservoirs (e.g., Ding et al., 2012; Reijers and Bartok, 1985). Fracture systems can be investigated across numerous scales, including seismic (Liu and Martinez, 2014; Pérez et al., 1999), dynamic field data (Ozkaya and Richard, 2006), outcrop analogues (Agosta et al., 2010; Guerriero et al., 2013), well data (Khoshbakht et al., 2012; Xu and Payne, 2009) and laboratory tests (Jones, 1975).

Outcrops are important to bridge the gap from regional seismic data to well-based data sets, as outcrops facilitate the mapping of fracture set relationships and fracture length. Within the past decade, tremendous advances have been made to facilitate the construction of digital outcrop models (DOMs) using Lidar-scanning (Buckley et al., 2008), photogrammetry (Carrivick et al., 2016; Smith et al., 2016; Westoby et al., 2012) and DEMs and satellites photos (Hodgetts et al., 2004; Pringle et al., 2001). Photogrammetry-based DOMs are cost-effective to acquire, requiring only a camera and processing software. By including ground control points, or global positioning systems (GPS)-positioning on the camera, high-resolution and spatially extensive DOMs can be acquired

* Corresponding author. Equinor ASA, Margrethe Jørgensens vei 13, 9406, Harstad, Norway.
E-mail address: klarssen@hotmail.com (K. Larssen).

https://doi.org/10.1016/j.marpetgeo.2020.104703
Received 26 April 2020; Received in revised form 3 September 2020; Accepted 5 September 2020
Available online 8 September 2020

and processed efficiently. Drone-deployed cameras are in particular useful to construct DOMs of the often very steep carbonate-dominated outcrops. DOMs can be used in fracture characterization (Casini et al., 2016; Larssen, 2018), mapping of sedimentary and igneous bodies (Chesley et al., 2017; Galland et al., 2019; Howell et al., 2014 and references therein) or as input for seismic modelling (Rabbel et al., 2018). It is notable that there is a shift from large-scale heli-Lidar acquisition campaigns (Rittersbacher et al., 2013) to more flexible and cost-effective drone-based photogrammetry surveys.

DOMs are applicable in many geological settings, but especially useful to characterize the notoriously heterogeneous carbonates. Furthermore, DOMs are ideally integrated with ground-based structural and sedimentological data, both for quality control and to extend the spatial significance of the collected field observations. There are different workflows documented in scientific literature that link DOMs to field observations, providing a foundation for constructing

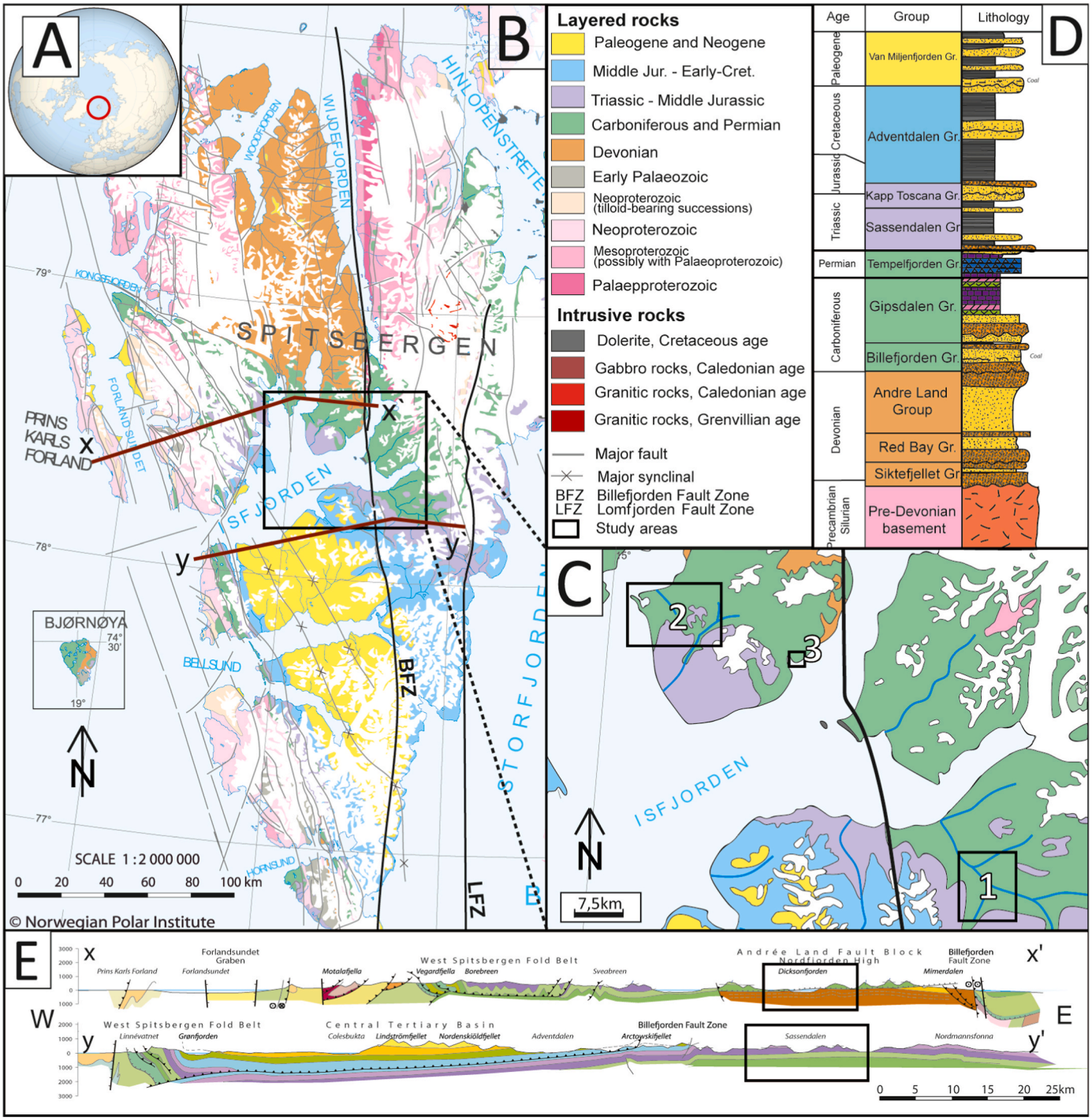

Fig. 1. Overview of the bedrock geology of the study area. A) Location of the Svalbard archipelago. B) Geological map of Spitsbergen. C) Location of the three different study areas (in black, 1. Sassendalen, 2. Southern Dickson Land, 3. Skansen, detailed locations indicated in Fig. 5) in central Spitsbergen. D) Simplified stratigraphic column highlighting the stratigraphic level targeted by this study (red box), redrawn from an unpublished figure by Arild Andersen (UiO). E) Regional cross-sections cutting through two of the study areas (study area highlighted in black boxes). Cross-sections and maps are courtesy of the Norwegian Polar Institute (Dallmann, 2015). (For interpretation of the references to color in this figure legend, the reader is referred to the Web version of this article.)

meaningful geology-driven models (e.g., Bisdom et al., 2017; Enge et al., 2007; Pringle et al., 2006; Wuestefeld et al., 2016).

In this contribution, we present a workflow that integrates field observations (structural and sedimentological data) with DOMs and use these to construct a realistic static geo-model of a dual porosity-dual permeability system. We illustrate the workflow by investigating a Middle to Upper Permian carbonate-dominated succession in central Spitsbergen, Svalbard.

2. Geological setting

2.1. Tectonic framework

Svalbard is a Norwegian high Arctic archipelago located between 74° and 81° north and 10°–35° east (Fig. 1). Svalbard represents the uplifted northwestern corner of the Barents Shelf and is structurally bounded in the north by a steep passive continental margin facing the deep Eurasian Basin (Faleide et al., 1984), whereas the previously rifted and now passive western margin divides Spitsbergen from the Knipovich Ridge, a transform segmented spreading ridge in the Norwegian-Greenland Sea (Talwani and Eldholm, 1977). Thermal uplift during Early Cretaceous (e.g., Døssing et al., 2013), rift shoulder uplift with transform movement during the Paleogene (Dallmann et al., 1993; Leever et al., 2011) and the development of a rifted margin contributed to the emergence of Svalbard and the adjacent northwestern Barents Shelf margin (Fig. 2) (Dimakis et al., 1998).

The regional tectono-stratigraphic evolution of Svalbard and the northern Barents Shelf is thoroughly described in previous contributions (Dallmann, 2015; Harland, 1997; Henriksen et al., 2011; Smelror et al., 2009; Worsley, 2008). The tectonic framework of Svalbard is constrained by N–S oriented long-lived fault lineaments (Steel and Worsley, 1984). The post-Caledonian tectonic evolution of Svalbard may be briefly summarized by the following regional tectonic events: (1) Devonian extension followed by compression (i.e. the Svalbardian event); (2) middle Carboniferous extension; (3) Late Paleozoic to Mesozoic platform subsidence; (4) late Mesozoic magmatism and thermal uplift; (5) Paleogene transpression, followed by transtension, and (6) regional Cenozoic exhumation. In addition, Svalbard continuously drifted northward from equatorial latitudes in the Ordovician to its present polar latitude (Worsley, 2008; Worsley et al., 1986). Several of these major tectonic events have directly influenced the development and evolution of the fracture system documented in this study (Fig. 3).

Middle Carboniferous extension led to the development of a series of N–S-elongated rift basins across Svalbard, as exemplified by the Billefjorden Trough (Bælum and Braathen, 2012; Johannessen and Steel, 1992; Smyrak-Sikora et al., 2019). In Late Carboniferous to Early Permian times, Svalbard continued to drift northward in concert with post-rift subsidence, resulting in the establishment of a shallow and

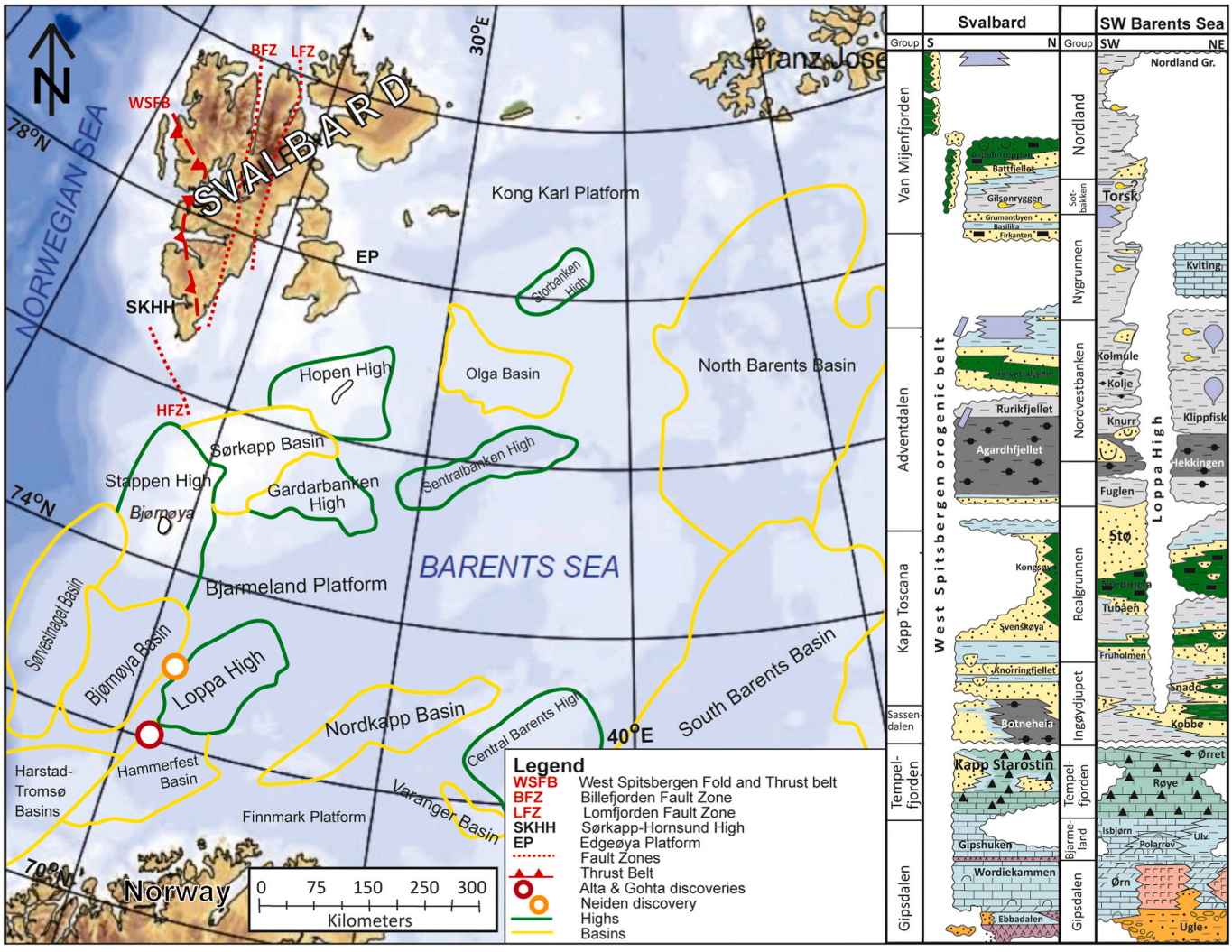

Fig. 2. The main structural elements on the SW Barents Shelf and Svalbard. Location of the carbonate discoveries, Alta,Gotha and Neiden, are indicated on the map. Map modified from Smelror et al. (2009). Lithostratigraphy adapted from Gradstein et al. (2010).

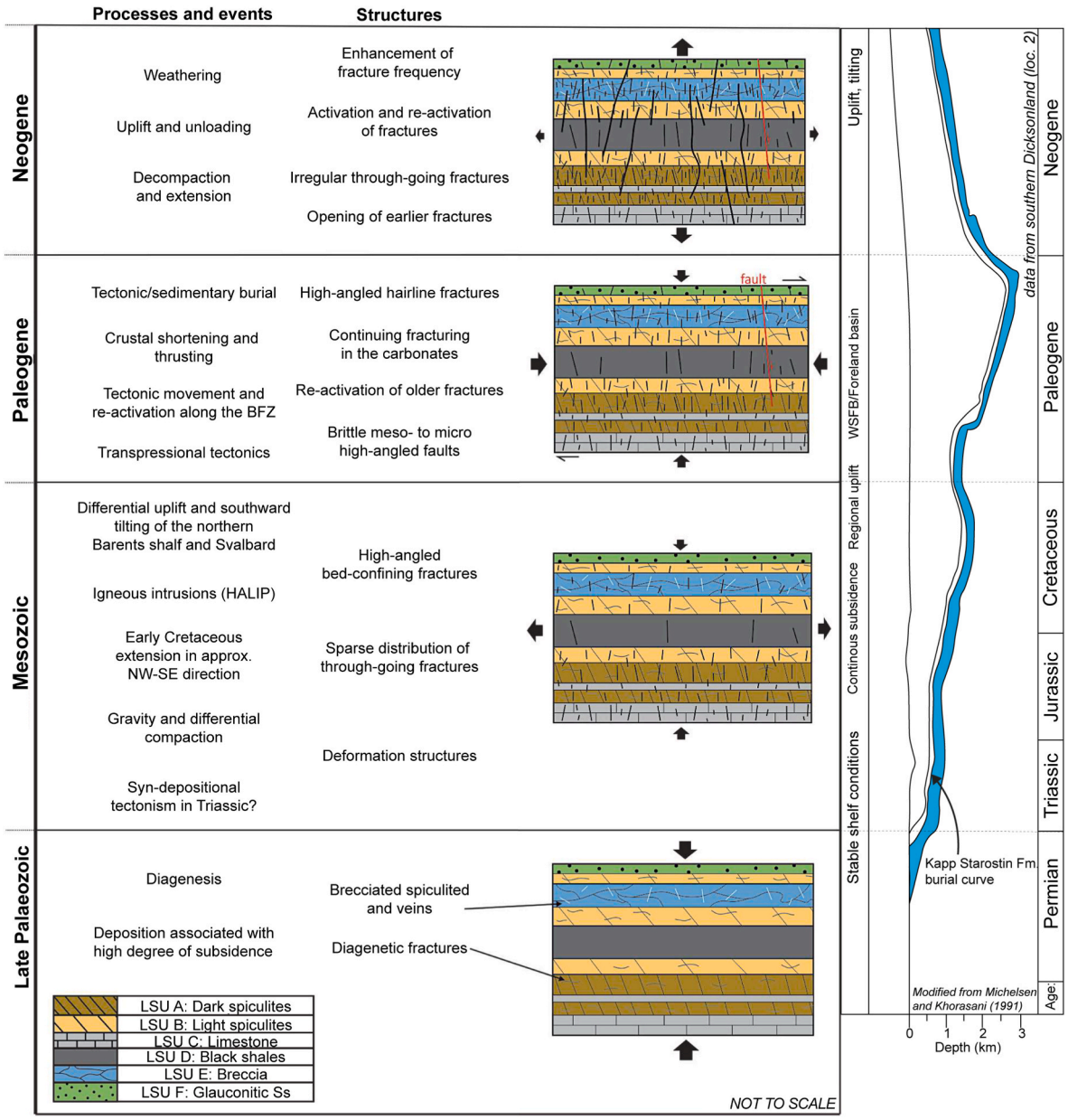

Fig. 3. Conceptual model illustrating how the fractures and fracture densities developed in the Kapp Starostin Fm. from deposition in Middle-Late Permian to present day. A detailed discussion of the tectonic events and processes for fracture development is provided in Larssen (2018). Burial curve (right) modified from locality 2 in Michelsen and Khorasani (1991), based on reflectance of coals from Devonian-Cenozoic.

periodically emerged warm-water carbonate platform (Blomeier et al., 2009; Sorento et al., 2020; Stemmerik, 2000; Worsley, 2008). Tectonically stable platform conditions continued into the Middle and Late Permian period. Although, Svalbard experienced gradual deepening and climatic cooling with the onset of widespread biogenic silica production (Blomeier et al., 2011).

Despite several MSc-theses (Larsen, 2010; Larssen, 2018; Strand, 2015), there are no peer-reviewed studies characterizing and quantifying the fracture system of the Tempelfjorden Group. Matysik et al. (2018) have linked parts of the observed fracture pattern and cement fills in the Kapp Starostin Formation spiculites to Cretaceous volcanism and Paleogene tectonism. The same authors attribute the undulating and anastomosing fracture pattern in the spiculites to silicification processes. Although the present contribution focuses on the workflow, the origin of the fracture system is briefly mentioned in relation to some of the tectonic events summarized in a conceptual model for fracture development in the Kapp Starostin Formation (Fig. 3). The fractures in this study are assumed to mainly be of tectonic and diagenetic origin and comprise steep irregular joints. The earliest fractures are a result of the deposition and diagenesis of the Kapp Starostin Formation during Upper Paleozoic (Fig. 3). The sediments were affected by diagenesis during early burial of the carbonates (Davies, 2005; Ehrenberg et al., 1998). This led to brittle fracturing of the spiculites by compaction deformation and stabilization of the silica (Matysik et al., 2018). During the Mesozoic, the first phase of NW-SE oriented seafloor spreading in the Arctic Ocean occurred, leading to volcanic activity (Døssing et al., 2013) and the development of igneous intrusions on central Spitsbergen (High Arctic Large Igneous Province, HALIP, e.g., Polteau et al., 2016; Senger et al., 2013; Senger et al., 2014). The extension also resulted in tectonic movements along the Billefjorden Fault Zone (BFZ) (Haremo et al., 1990; Harland et al., 1974). Most of the fractures in this study are interpreted to have originated during the tectonic setting in Paleogene (Fig. 3). Transpressional and transtensional stress related to the development of the West Spitsbergen Fold and Thrust Belt (WSFB, for references see (Bergh et al.,

1997; Braathen et al., 1999) are assumed to be the main event for fracture generation. Uplift and unloading during the Neogene (Dörr et al., 2013) led to the development and opening of the large through-going (TG) fractures along existing discontinuities (Fig. 3). For a full discussion of the development of the fracture system in the Kapp Starosin Formation, the reader is referred to Larssen (2018).

2.2. Lithostratigraphy

The tectonically stable platform conditions characterized Svalbard and the northern Barents Shelf throughout the Permian. The middle–Upper Permian Tempelfjorden Group is an up to c. 450 m thick succession of spiculites, siliceous shale and shallow marine carbonates of cool-water affinity (Blomeier et al., 2011, 2013; Ehrenberg et al., 2001). The succession records regional subsidence and rapid deepening of the previous shallow and partly emerged platform area, possibly induced by the onset of the Uralian orogeny (Worsley, 2008).

Throughout central Spitsbergen and Nordaustlandet, the Middle to Upper Permian Tempelfjorden Group consists mainly of the Kapp Starostin Formation. Age- and facies-equivalent strata in the subsurface of the Barents Shelf are also assigned to the Tempelfjorden Group (e.g. the Røye and Ørret formations on the Loppa High and Finnmark Platform) (Fig. 2). The Kapp Starostin Formation is thinning to the NE where it displays more proximal facies (Blomeier et al., 2013; Bond et al., 2017; Ehrenberg et al., 2001; Worsley et al., 1986). In southern Dickson Land, where the main section of this study is located (Fig. 1C), the formation is c. 180 m thick. The thinning of strata against structural highs (Bond et al., 2017; Ehrenberg et al., 2001; Worsley et al., 1986) indicates draping over pre-existing topography inherited from Middle Carboniferous rifting and Late Carboniferous post-rift subsidence. Several publications assess the detailed facies distribution and sequence stratigraphic arrangement of the Kapp Starostin Formation (Blomeier et al., 2011, 2013; Ehrenberg et al., 2001; Ezaki et al., 1994; Hüneke et al., 2001; Malkowski, 1982; Matysik et al., 2018). Therefore, we only provide a brief facies overview.

The lowermost part of the Kapp Starostin Formation consists of a c. 40 m thick sheet-like bioclastic unit of regional extent referred to as the Vøringen Member. The unit is dominated by brachiopod limestone, with subordinate amounts of crinoid and bryozoan fragments. The base of the unit marks a regional unconformity separating the Tempelfjorden Group from the underlying warm-water carbonates of the Lower Permian Gipsdalen Group (not considered here). The unit is interpreted to represent a transgressive shallow marine deposit, following a long-lasting subaerial exposure of the shelf (Blomeier et al., 2013; Sorento et al., 2020; Uchman et al., 2016). The Vøringen Member grades upward into dark-colored spiculites and siliceous shales, recording a regional long-term transgressive development. Several intercalated fossiliferous limestone units consisting of partly silicified brachiopod, bryozoan and crinoid wacke-to packstones occur. These upward-shoaling limestone units record high-frequency regressive pulses superimposed on the transgressive development (Blomeier et al., 2013; Bond et al., 2017). In the upper part of the formation, particularly towards the basin margin and in proximity to palaeo-highs, shallow-marine light-colored spiculites and glauconitic sandstones become more abundant. They record shorter periods of localized uplift. The Permian–Triassic boundary marks the end of the Paleozoic carbonate platform and the onset of the Mesozoic siliciclastic shelf development (Uchman et al., 2016; Wignall et al., 1998; Worsley, 2008).

The Tempelfjorden Group has been subject to little successful exploration and drilling campaigns along the margins of the Loppa High and on the Finnmark Platform (Larssen et al., 2005). The only exception is the combined Alta and Gotha discovery on the Loppa High, and the Neiden discovery further north (Fig. 2). Here, the reservoir also includes warm-water carbonates of the underlying Gipsdalen Group. The Permian succession has been intensely karstified by meteoric water as past uplift events exposed the Loppa High (e.g., Ahlborn et al., 2014). Other oil-discoveries on the Barents Shelf have been linked to an Upper Permian oil-prone source rock, possibly originating from organic-rich shales within the Ørret Formation (Lerch et al., 2016). No such viable source rock unit has, to date, been reported from the Tempelfjorden Group in Svalbard (e.g., Nicolaisen et al., 2019).

3. Methods and data

Sedimentological and structural field data were collected during fieldwork in April and August 2018 in central Spitsbergen, Svalbard (Fig. 1, Table 1). These traditional field observations were complemented by extensive digital photographing of outcrops for constructing 3D DOMs (Table 2). The DOMs were used for additional structural analyses. The rock samples were used for pore analysis from thin section studies. Structural field and digital data were integrated to construct a discrete fracture network model.

Numerous software packages were utilized in this study and are listed in Table 3.

4. Results

4.1. Workflow: from outcrop to geo-model

Fig. 4 illustrates a flowchart describing the overall workflow from field data collection to geomodelling, upscaling and applications.

4.2. Field observations

Fieldwork primarily provides sedimentological (logging and sampling) and structural (scanlines and window sampling) data.

4.2.1. Sedimentology

Lithological data were acquired through sedimentological logging and interpretation from 3 different locations (Esperantodalen south (referred to as the E_S), Idodalen north A (Id_N_a) and Heimenfjellet waterfall (Hf_w) (Fig. 5) resulting in a 178 m composite log (Fig. 6). The logging resulted in the description of 12 different sedimentary facies, each distinguished by contrasting lithologies, colors, fossils, mechanical properties and fracture pattern. A detailed description is presented in Table 6(Appendix A). The log is also divided into zones. Each zone represents a lithological section measured in field, and zones that contain structural orientation data are indicated in the log by grey color (Fig. 6).

Logging was conducted in several locations due to inaccessible steep terrain and scree covering layers. The sedimentary facies presented in the log can be correlated with several outcrops in the area. Based on the great similarities in terms of vertical distribution of the facies and distinct beds, the strata cropping out in Idodalen is understood to represent the same lateral equivalent strata as in Esperantodalen (Fig. 6). Based on this assumption, detailed logging has not been conducted in all parts of Idodalen and zones and facies have been correlated with each other.

4.2.2. Fracture systems

Structural characterization and fracture set determination is based on scanlines, i.e. the line-intersection method (Ogata et al., 2014; Rohrbaugh et al., 2002; Singhal and Gupta, 2010) and fracture window sampling (Belayneh et al., 2009; Watkins et al., 2015; Zeeb et al., 2013). Fractures were measured using a compass with clinometer or an iPhone 6S with the Fieldmove Clino app (Vaughan et al., 2014) and classified as either bed-confined (BC) or through-going (TG). The scanline method samples fractures along a straight line (line represented by a measuring tape) crossing the outcrop or parts of it. Every fracture is recorded with distance from scanline origin, orientation (dip/dip direction), fracture length, aperture, BC/TG and additional comments. The data is compared with bed orientation and bed thickness to quantify fracture spacing and

Table 1
Summary of data types and methods. SfM = Structure-from-motion, i.e. photogrammetry.

Data type	Method	Purpose	Quantity (n)	Comments
Composite log	Sedimentological logging	Constrains fractures to lithology	1	Total length of 178 m, logged at 1:100 scale at 3 different locations
Digital photos	Digital outcrop modelling	Outcrop and structural analyses	3119	Georeferenced digital photos taken with Nikon D5300 (24.3 MP) with a 50 mm Sigma lens
Digital outcrop models	Construction of 3D photogrammetric mage (DOM)	Facilitate virtual measurement on entire outcrop	10	Processed by SfM photogrammetry
Structural measurements	Manual fracture measurements in field	Fracture orientation data	5529	Mapped fractures using a compass
	Manual fracture measurements in LIME software	Fracture orientation data	360	Manual fracture mapping using LIME software
	Automatic fracture measurements in PlaneDetect software	Fracture orientation data	6909	Automated fracture mapping using PlaneDetect software
Digital scanlines	Scanlines and measurements on DOM	Fracture spacing in inaccessible sites	26	Measurements from photogrammetry
Scanlines	Line survey in outcrop	Fracture spacing and frequency	7	Collected in field
Geo-model	Facies and petrophysical modelling using Petrel	Build a geo model for fracture modelling	2	Input from composite logs and thin sections
Discrete fracture network model	Fracture modelling using Petrel	Modelling of fracture networks	3	Based on multi-scale field data
Carbonate thin sections	ImageJ analysis of thin section images	Estimate matrix porosity	10	Based on rock samples

Table 2
Summary of the 10 processed digital outcrop models.

Locality	Latitude	Longitude	Number of photos	Outcrop extent (m)	Outcrop orientation	Outcrop facing
Brattlidalen C	78°17′48″	17°10′11″	243	19,5	E-W	N
Brattlidalen E	78°17′49″	17°10′07″	228	12,5	NW-SE	NE
Brattlidalen F	78°17′49″	17°09′47″	283	7,5	NNE-SSW	SSE
Brattlidalen G	78°17′49″	17°09′56″	263	10	WNW-ESE	NNE
Eskerfossen east	78°14′50″	17°03′32″	378	13,5	N–S	W
Eskerfossen north	78°15′01″	17°03′39″	459	20,5	WNW-WSW	SSE
Esperantodalen north	78°36′36″	15°27′29″	45	233	NW-SE	SW
Esperantodalen south	78°36′42″	15°26′24″	324	570	NW-SE	NE
Heimenfjellet	78°35′07″	15°26′21″	164	25	NNW-SSE	SSW
Skansen	78°31′36″	16°03′51″	388	2543	NE-SW/NW-SE	SE/SW

Table 3
Summary of the software utilized in this study.

Software	Purpose	Comments	Reference
Agisoft Metashape	3D digital outcrop model processing	Georeferenced camera position, mm-cm pixel resolution	Casini et al. (2016)
LIME	Interpretation and manual mapping of fracture planes	Quantitative structural work	Buckley et al. (2019)
PlaneDetect	Automatic fracture plane mapping	Based on input from user	Lato and Vöge (2012); Vöge et al. (2013)
ImageJ	Porosity estimation from thin sections, digital scanlines	Input from fieldwork and DOMs	Larssen (2018); Senger et al., (2015)a,b, Grove and Jerram (2011)
Petrel (version 2016)	Geomodelling	Used for facies, petrophysical and fracture modelling	Schlumberger trademark
Fieldmove Clino	iPhone App for structural measurements in field	Preferred method for structural measurements	Vaughan et al. (2014)

frequency. Due to steep and challenging terrain, few scanlines were collected, and photogrammetry-based structural analyses were the primary source of structural data in this study.

4.3. Quantitative digital fieldwork

High-resolution, geo-referenced digital photos were acquired for photogrammetry, including modelling of ten 3D DOMs (Table 2) and fracture profiles from digital photos (Fig. 8). Photos acquired for virtual outcrops were taken using a Nikon D5300 (24.3 MP) with a Sigma fixed focal length (50 mm) lens. All the photos for the 3D digital models were georeferenced with the built-in GPS and taken at slightly different angles every 1–5 m along the outcrop. This is to obtain the best result when processing the data. Digital photos acquired in the field were pre-processed and processed to provide output data and model analyses. The pixel size of the DOMs in this study are 4 × 4 μm which provides the possibility to observe features on a cm-scale.

4.3.1. Virtual outcrop modelling from photogrammetry

Virtual outcrops were constructed using the software Agisoft Metashape Professional (version 1.3.3). All photos were pre-processed manually in the software to remove undesired areas and ensure the model is as noise-free as possible. Construction of the 3D model requires several processing steps. The processing starts by aligning the digital, geo-referenced photos (Fig. 7A, B), before constructing a sparse point cloud (Fig. 7C) by finding mutual points in two or more photos. Further processing includes generation of a dense point cloud (Fig. 7D) followed by meshing (Fig. 7E). The final processing step uses the digital photos to texture the outcrop (Fig. 7F) before it can be exported for further use.

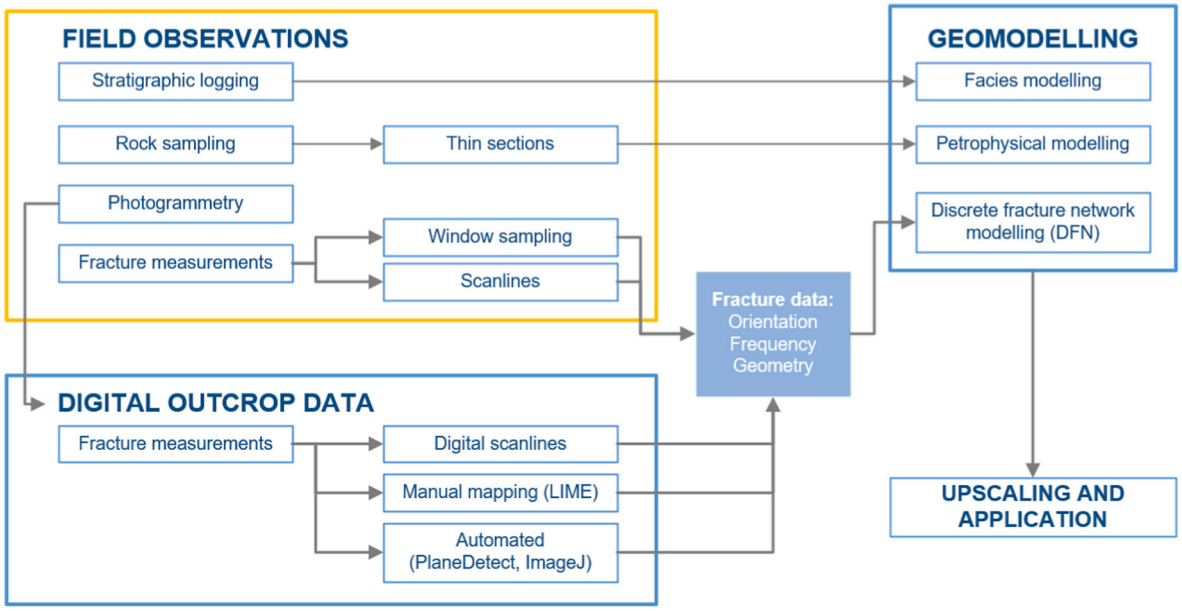

Fig. 4. Synthesis of the presented workflow, from outcrop to geo-model, illustrating field observations, digital outcrop data, geomodelling and finally upscaling and application.

4.3.2. *Digital scanlines*

In addition to traditional scanlines, several digital fracture spacing profiles (digital scanlines) were processed and analyzed to obtain fracture spacing (Fig. 8B). These profiles were made from digital photos or directly on the generated 3D models (Senger et al., 2015a). The fractures along the digital profiles were mapped using a drawing program and further analyzed using the software ImageJ. Fractures measured on digital scanlines are automatically corrected. Whereas fractures measured using the normal scanline method was corrected afterwards using the Terzaghi correction (Terzaghi, 1965). All scanlines are found in Table 7 (Appendix B).

4.3.3. *Digital outcrop visualization and quantitative analyzes of fractures*

LIME software (Buckley et al., 2019) was used to visualize the DOMs and measure distances, plane- and outcrop orientations (Fig. 8A). Automatic fracture mapping was conducted using PlaneDetect (Fig. 8C). PlaneDetect (Lato and Vöge, 2012; Vöge et al., 2013) automatically maps out fracture planes on the meshed surface model exported from Agisoft Metashape (Fig. 8A).

4.4. *Geomodelling*

4.4.1. *Reservoir properties from thin sections*

Ten thin sections were produced from rock samples collected from different facies (location indicated in Fig. 6) and were used for matrix porosity estimation using ImageJ. The resulting porosity values (Fig. 9, Table 4) were further used for petrophysical modelling with complementary data from Grundvåg (2008) who also used thin section studies for porosity analysis in similar study areas. However, it should be mentioned that the amount of thin sections in this study are limited and sparse, and this can a basic lack of statistical validation.

4.4.2. *Fracture characteristics*

In general, each facies comprises 1–3 fracture sets with steeply dipping fractures (Fig. 10B and C). The whisker plot (Fig. 10A), arranged after lithologies and localities, show that the overall mean fracture spacing in the carbonates is low. Orientation data from digital outcrop models (example from Eskerfossen south, Fig. 8D) show that the data from fieldwork correlates well with data extracted digitally. The data from virtual outcrops generally show less spread in orientations.

4.4.3. *Discrete fracture network (DFN) modelling*

The geo-model was generated using the Schlumberger Petrel modelling software (version 2016) and cell sizes were chosen to represent geological heterogeneities at different scales and enable computational efficiency. The model is tied to the sedimentological log which was divided into litho-structural units (LSU) based on similarities in matrix properties, mechanical behavior and sedimentary facies; dark spiculites (LSU A), light spiculites (LSU B), limestones (LSU C), black shales (LSU D), breccia (LSU E) and glauconitic sandstones (LSU F). These LSUs in the discrete well log make the base for the zones used in the geomodelling (Fig. 11D).

4.4.4. *Petrophysical modelling*

Property modelling was used to assign specific properties to each cell within the different zones. Porosity was assigned as a matrix property in each LSU based on data from the thin section analysis (Table 4). The matrix properties are considered to change vertically and are therefore modelled using a Gaussian Random Function Simulation (GRFS). Samples from various limestones and the black shales showed 0% matrix porosity and the highest matrix porosity was present in the glauconitic sandstones (20%) and light spiculites (10%).

Note that this is a simplistic approach and that porosity within a heterogenous rock varies based on the complexity of depositional setting and diagenetic overprint. In addition to porosity, fracture density was modelled as a general petrophysical property to show the distribution of densities within each LSU.

4.4.5. *Fracture modelling*

A fracture network was constructed by defining fracture sets as input for discrete fracture modelling. For each fracture set geometry, distribution, orientation and aperture were defined (Table 5). Input data for the different fracture sets were based on data acquired during fieldwork or from virtual outcrops. Thereafter, the data were assigned to the respective LSU that exhibits similar mechanical properties. All fracture sets obtained in the study are defined consistently based on their main orientations and comprise 7 fracture sets. All sets are identified to represent open to partly open fractures. Veins and filled fractures were also observed but have not been considered as an own fracture set due to the lack of statistics and the great dominance of open fractures.

The base case (2500 × 2500 × 245 m model) is mainly modelled

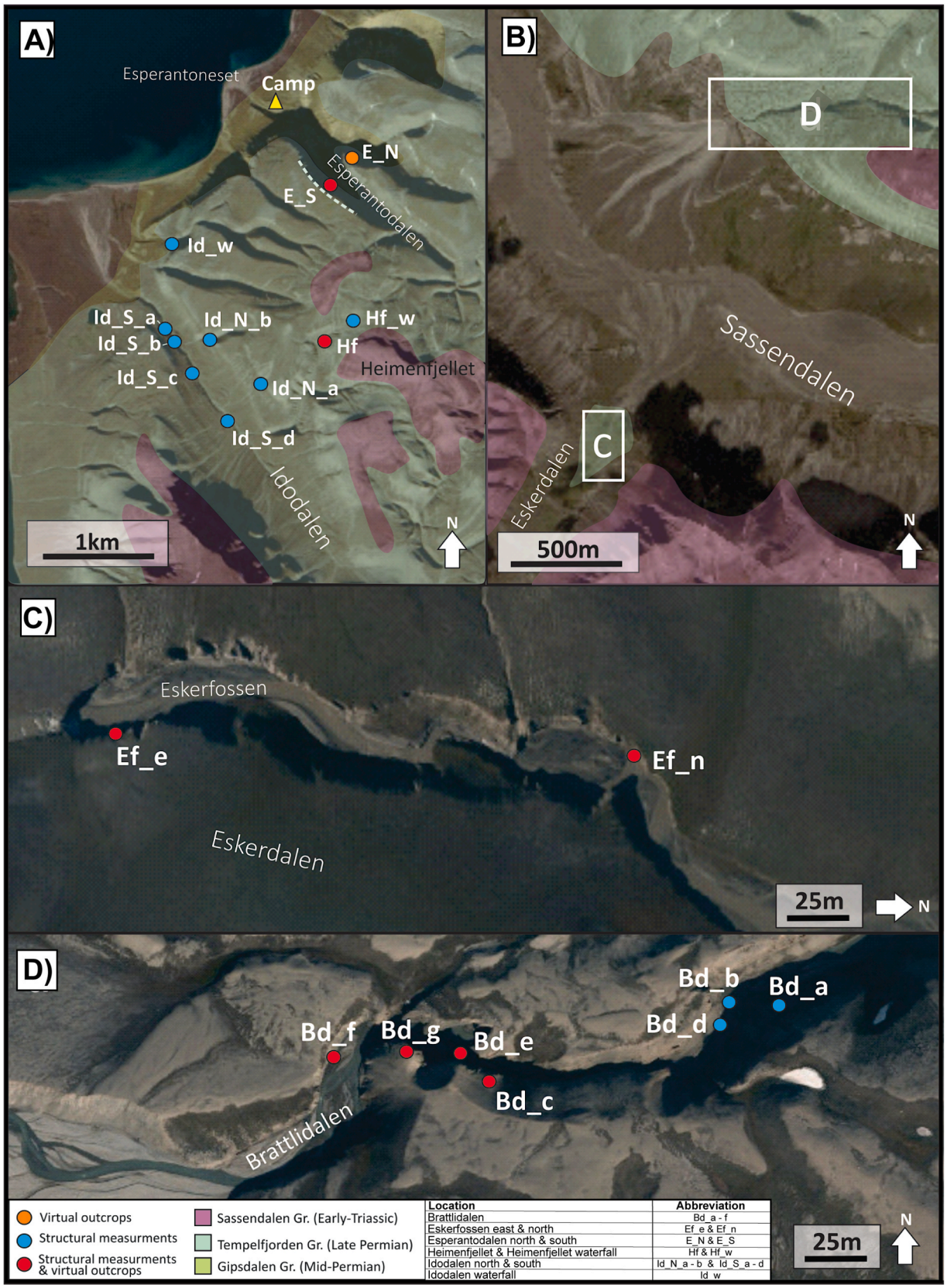

Fig. 5. Satellite images (toposvalbard.npolar.no) of the study sites. Location of the study areas on Svalbard are indicated in Fig. 1. A) map of the study area in southern Dickson Land, the dotted line in E_S represent the lateral area that was covered at the location. B) larger scale map of the Sassendalen area indicating the locations of C) Eskerfossen and D) Brattlidalen. Geology added from Svalbardkartet. Data courtesy of Norwegian Polar Institute.

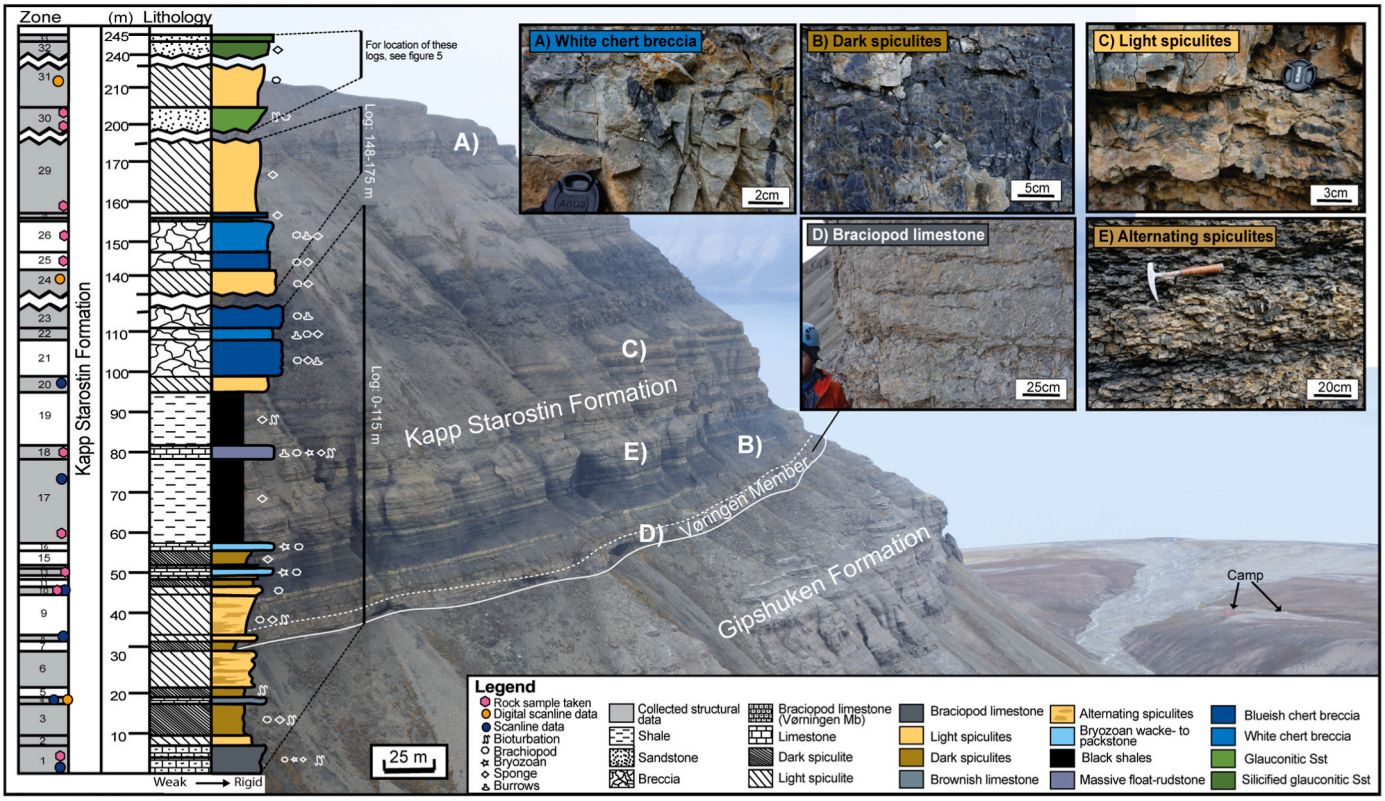

Fig. 6. The 178 m composite log is based on sedimentary logging from 4 localities in southern Dickson Land (Fig. 1). The zones in the log represent where orientation data have been acquired. The log displays the mechanical properties, not grain size. The main outcrop is shown here, Esperantodalen south (Fig. 5), where the boundary between the different formations are highlighted. A)-E) show photos taken in field from different facies.

with input parameters derived from field data. However, assumptions were made for geometry data and aperture, as these cannot be measured directly in field. Orientation and distribution data are purely based on the results from fieldwork, whereas aperture and geometry data are based on studies of other carbonates (Bisdom et al., 2016; Boro et al., 2014; Hardebol et al., 2015; Mäkel, 2007). The fracture network was modelled as implicit (fracture length is < 5 m) and discrete (fracture length is > 5m) fractures.

The geometry of fractures was kept constant with a mean fracture length of 1.5 m and a normal distribution of 1. Orientation was modelled using constant values for each fracture set with a Fisher distribution with a concentration of 100. Aperture was modelled with a normal distribution using a mean aperture and standard deviation of 0.1 mm. The fracture density for each fracture set was assigned based on P_{32} (Dershowitz and Herda, 1992), a scale-independent parameter that relates the cumulative fracture area to the volume (m^2/m^3).

4.5. Upscaling and applications of fracture model

The fracture network was upscaled using the Oda-method (Oda, 1985) which generated a series of properties for the fracture network such as fracture porosity (frac_poro) and fracture connectivity (fracture-matrix coupling parameter, frac_sigma) (Fig. 11E). The sensitivity of the different parameters was tested using a synthetic grid model of 50 × 50 × 50 m with 125 000 1 × 1x1 m cells and for each input parameter 10 cases were modelled, in addition to a base case that was purely based on outcrop data (Fig. 12). To investigate which LSU exhibits the best reservoir properties (i.e. overall porosity and fracture connectivity), a model of 100 × 100 × 120 m, 20 × 20 × 1 m sized cells was modelled. The base case model was implemented with field data as representative inputs; fracture length of 1.5 m, aperture of 0.1 mm, and P_{32}, fracture density of 15 m^2/m^3.

5. Discussion

5.1. Fracture porosity: controlling parameters

The results (Fig. 11E) indicate highest fracture porosity in the dark spiculites and the lowest fracture porosity in black shales and glauconitic sandstones. The fracture connectivity is highest in the lower part of the formation, under the black shales. The four TG fracture sets were modelled together with all bed-confined fracture sets in a supplementary fracture network to investigate how they affect the fracture connectivity (rightmost column Fig. 11E). The result suggests a low impact on the overall fracture connectivity. In addition to matrix porosity, fracture porosity (P33, Dershowitz and Herda, 1992) contributes to secondary porosity in the carbonates. Sensitivity tests (Fig. 12) show a mean fracture porosity in the base case of around 0.38%. Fracture porosity of 1% will not be achieved unless the fracture aperture exceeds 0.5 mm (base case 0.1 mm) or the fracture density is around 40 m^2/m^3 (base case 15 m^2/m^3). The results suggest that fracture length only plays a minor role in the studied 0.1–250 m range (base case 1.5 m). Fracture porosity, however, is greatly affected if the mean fracture aperture or the fracture density increases. The sensitivity tests of the DFN focus on quantifying the impact of fracture density, aperture and length variations on the DFN model. A primary fracture porosity range close to 1% is recorded in the fractured carbonates, typically around 0.05–0.5%. Results from published literature about fracture porosity suggest similarities; Kim and Schechter (2009) used a fractal discrete fracture network and indicated fracture porosities from 0.0001 to 0.1%, whereas semi-log calculations of fracture porosity from pressure data suggest 0.14% (Tiab et al., 2006). As illustrated by the results in this study, the fracture porosity is strongly related to the fracture aperture and/or density. Similar results have been documented by Senger et al. (2015b) for an unconventional siliciclastic reservoir projected for CO_2 sequestration in central Spitsbergen. Their

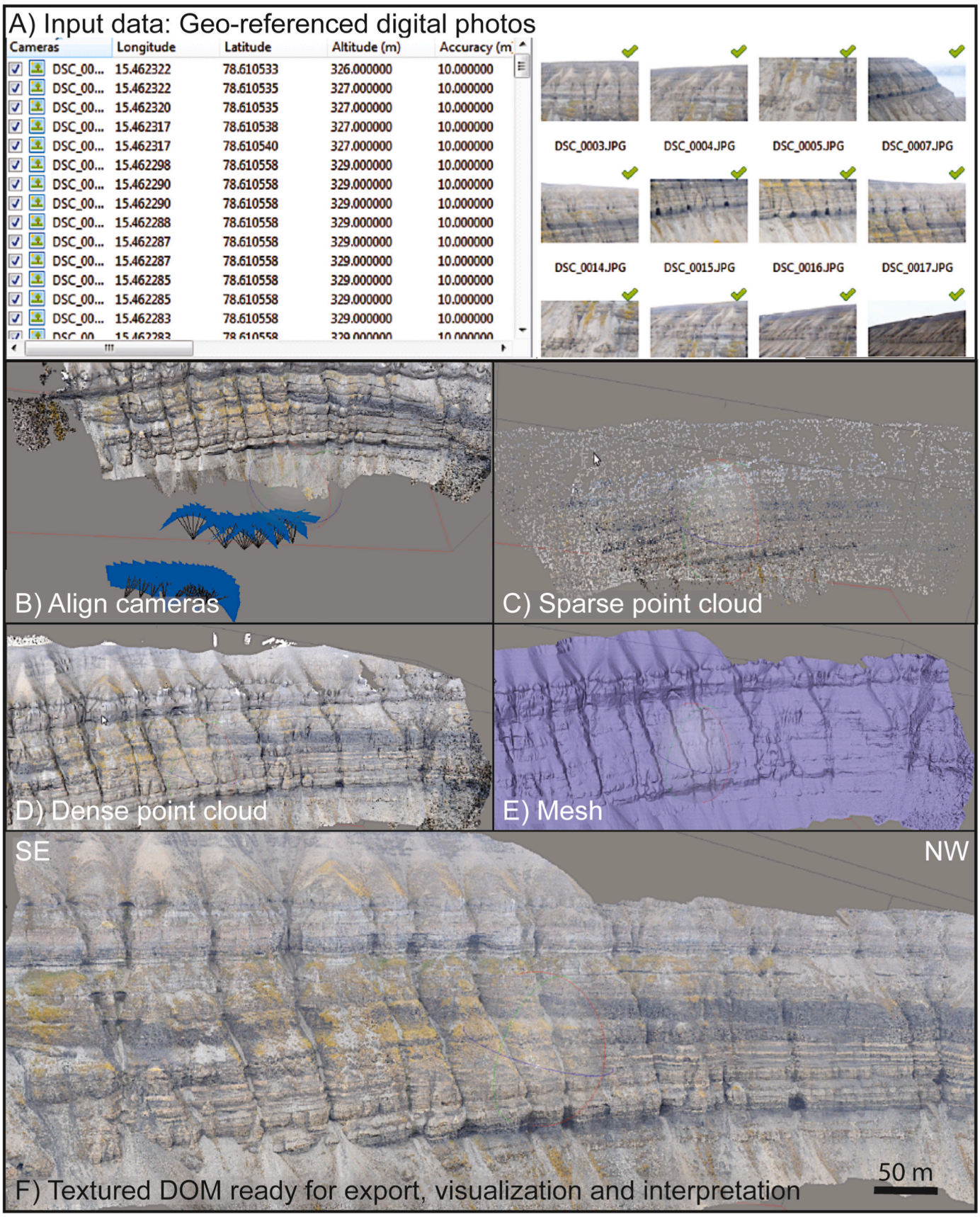

Fig. 7. Workflow describing the different steps conducted in Agisoft. A) and B) represent pre-processing steps, while C) to F) are showing the various processing steps to get a complete textures 3D model ready for export and further use.

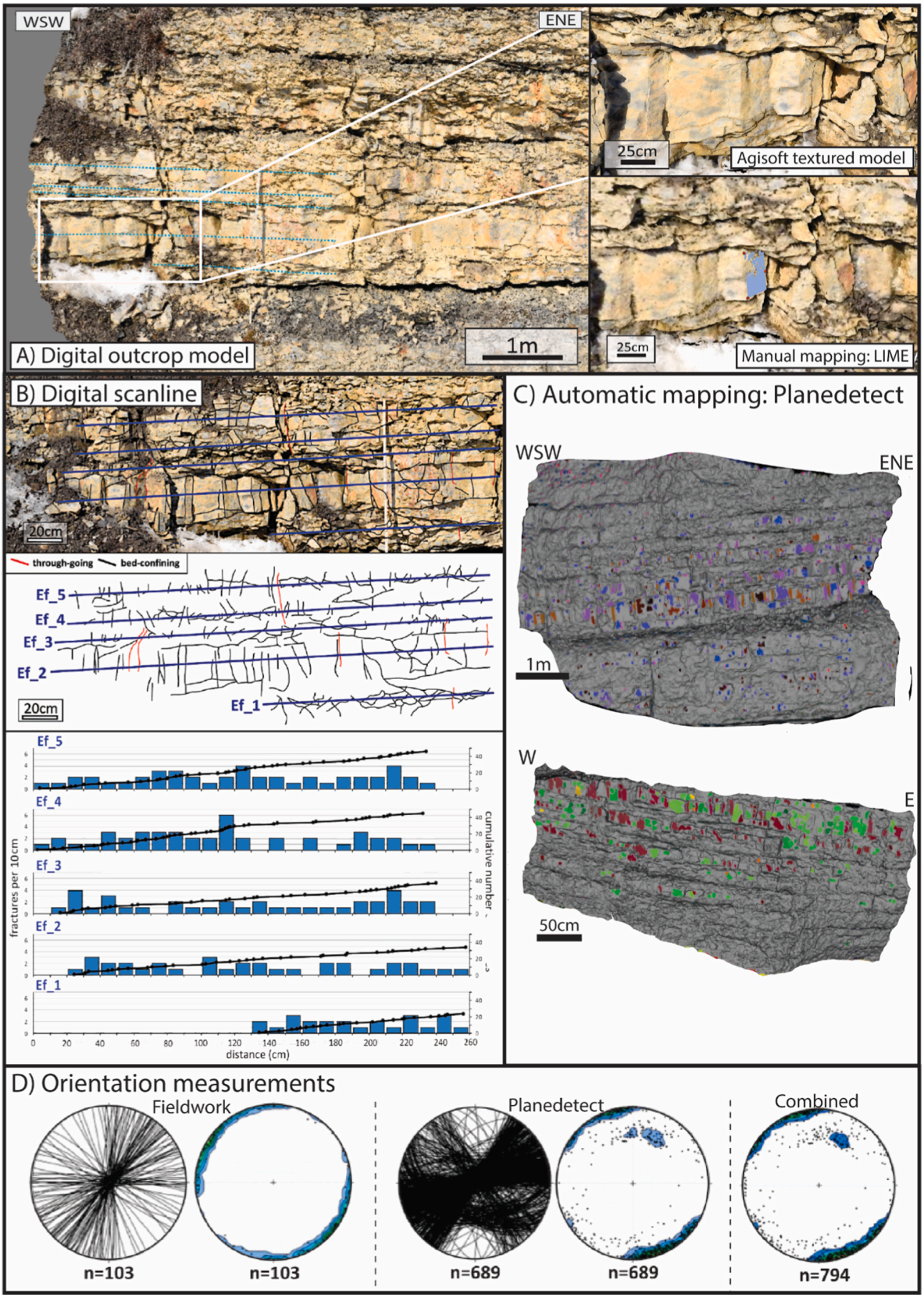

Fig. 8. Examples from the Eskerfossen north (Ef_n) outcrop. A) The digital outcrop model showed good quality after texturing, before exporting the model for manual mapping in LIME. B) 5 digital scanlines were acquired from the 3D model. C) PlaneDetect were used on two different parts of the whole outcrop for automatic mapping. The uppermost model is the same as in A) and B). D) Comparison of orientation measurements from traditional field mapping and automatic mapping in PlaneDetect.

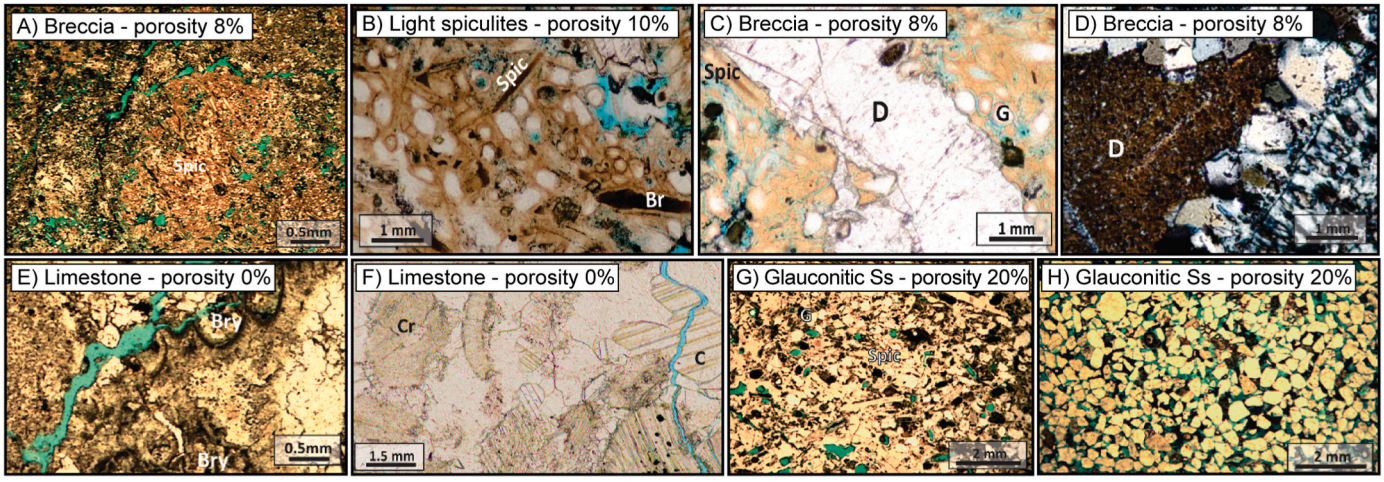

Fig. 9. Examples from the thin section study for matrix porosity measurements. Respective facies and measured porosity are indicated. Blue epoxy indicates porosity. E) and F) with 0% matrix porosity, but as shown by blue epoxy, they have open fractures. D = dolomite, G = glauconitic grains, Spic = spiculites, Cr = crinoid, Br = brachiopod. (For interpretation of the references to color in this figure legend, the reader is referred to the Web version of this article.)

Table 4
Matrix porosities assigned as properties within the different lito-structural units defined for modelling.Complementary data from Grundvåg (2008).

		Porosity (%)				
LSU	Facies	Min	Mean	Max	Method	Data from
A	Dark spiculites	0	2	5	GRFS	Grundvåg (2008)
B	Light spiculites	5	10	20	GRFS	Grundvåg (2008)
C	Limestones	–	0	–	Assign	This study
D	Black shale	–	0	–	Assign	This study
E	Breccia	1	8	15	GRFS	This study
F	Glauconitic Ss	5	20	30	GRFS	This study

results indicated increasing trends with increasing fracture aperture or fracture densities. However, Boro et al. (2014) indicate that the fracture porosity is only showing minor variations when changing the aperture. The fracture porosity is a function of the fracture spacing and the aperture and can be difficult to determine and model (Mäkel, 2007). Fracture porosities are assumed to be most important in reservoirs with poor matrix properties. Therefore, in reservoirs with reasonable matrix permeabilities and good matrix storage capacities, the value of fracture porosity is irrelevant (Mäkel, 2007). However, Witherspoon et al. (1980) state that fracture porosity will always be an important parameter as it is determining the fracture permeability.

The use of a small-scale synthetic fracture model allows for several fracture realizations and upscaling. It is important to take the uncertainties connected to fracture network characterization into account. By preforming sensitivity testing, the most suitable results from upscaling can be acquired and further used as input in a dual-porosity dual-permeability model of reservoir-scale or flow simulation. The sensitivity analysis conducted by Boro et al. (2014) also presents the impact of other fracture variations that have not been investigated in this study. In addition to variations of fracture aperture, their emphasis lay on variations connected to thickness of fracture units, the fracture shape and dispersion level on fracture orientations. These results suggest that changing the dispersion level of orientations, the fracture shape or fracture unit thicknesses have minor to none influence on the fracture porosity used in their base case.

5.2. *Digital outcrop model acquisition, processing and interpretation: reflections on best practice*

Good planning is crucial to collect data for a good DOM that is fit for its purpose (e.g., Sturzenegger and Stead, 2009). Outcrops to be used for

Table 5
Input parameters for the base case model and downscaled LSU model.

Fracture set	Distribution	Orientation			Aperture		
	Density value (P_{32}, m^2/m^3)	Mean dip(°)	Mean dip azimuth (°)	Concentration	Aperture width (mm)	Std. Dev.	Max
LSU A - 1	21	88	68	100	0.1	0.0015	0.25
LSU A - 2	23	89	35	100	0.1	0.0015	0.25
LSU A - 3	19.5	88	155	100	0.1	0.0015	0.25
LSU B - 1	13.1	89	74	100	0.1	0.0015	0.25
LSU B - 2	15.75	89	155	100	0.1	0.0015	0.25
LSU C - 1	10.6	88	67	100	0.1	0.0015	0.25
LSU C - 2	11.44	86	161	100	0.1	0.0015	0.25
LSU D - 1	4	87	243	100	0.1	0.0015	0.25
LSU D - 2	6.63	89	338	100	0.1	0.0015	0.25
LSU E - 1	9	89	320	100	0.1	0.0015	0.25
LSU E - 2	13	87	72	100	0.1	0.0015	0.25
LSU E - 3	11.5	89	333	100	0.1	0.0015	0.25
LSU F - 1	6.5	89	250	100	0.1	0.0015	0.25
LSU F - 2	5.75	89	334	100	0.1	0.0015	0.25
TG sets							
TG - 1	0.1	86	104	100	0.1	0.0015	0.25
TG - 2	0.051	89	325	100	0.1	0.0015	0.25
TG - 3	0.2	82	81	100	0.1	0.0015	0.25
TG - 4	0.15	84	193	100	0.1	0.0015	0.25

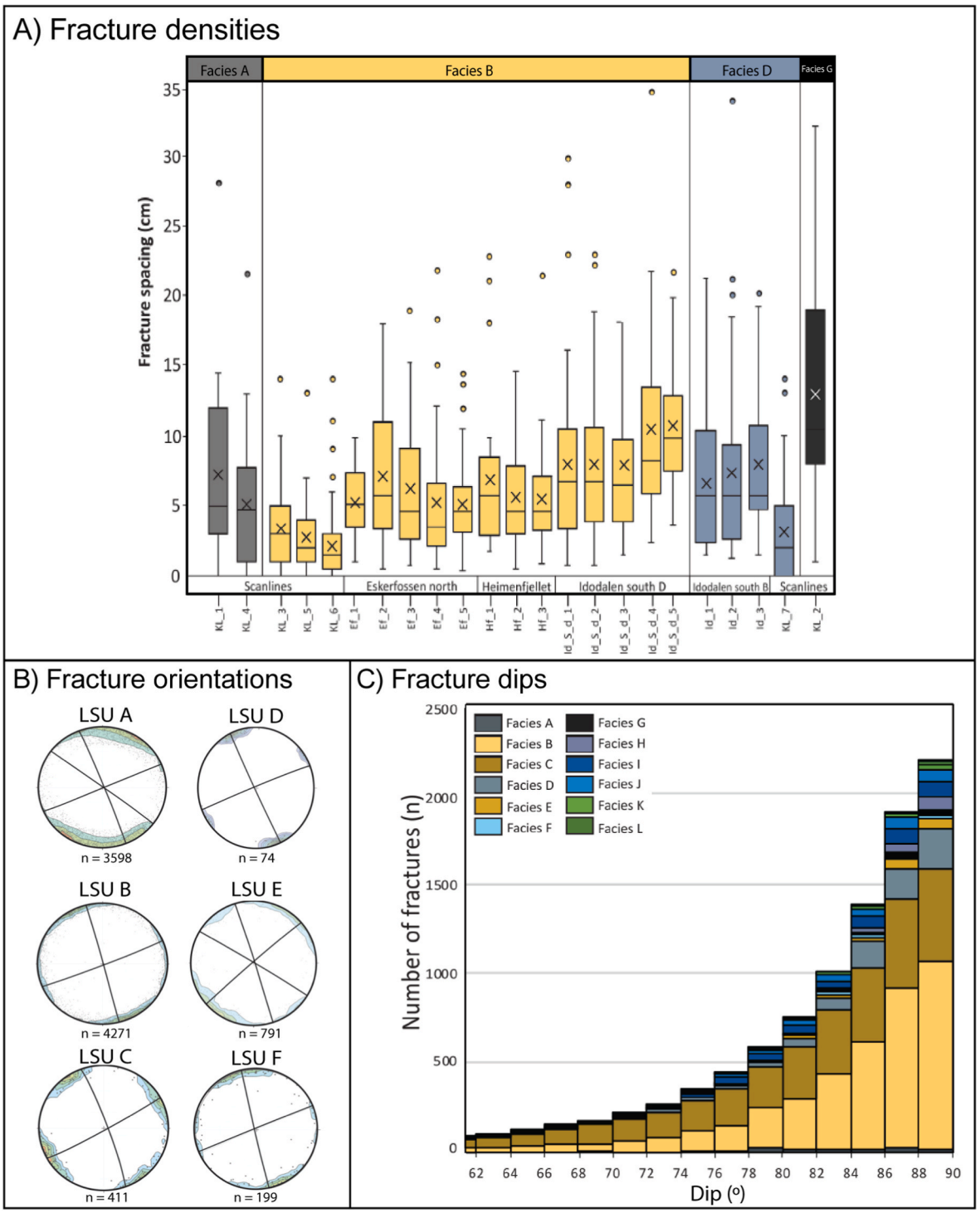

Fig. 10. A) Whisker plots (minimum, lower quartile, mean, upper quartile) of fracture spacing for scanlines and digital profiles divided based on lithology and partly localities. Facies A is referred to as brachiopod limestone, facies B is light spiculitic cherts, facies D is brownish limestone and facies G is black shales. B) Fracture sets used as input for the geo-model. Orientations for the different LSU's are listed in Table 5. C) Histogram summarizing all the dips from the fracture measurements, divided by facies. The plot indicates that the fractures in this study are mainly high-angled. All units show an increasing trend with the most fractures dipping between 88° and 90°.The bin size is 2°.

interpretation of large-scale structures, such as faults, large fractures, folds, will work well using photogrammetry even when obtained from a larger distance with a lower number of photos (Senger et al., 2015a). The DOMs used for large scale interpretation in this study showed good and enough quality for its purpose (i.e. Skansen, Esperantodalen). Experiences here show that it is not necessary to have a high number of high-resolution digital photos to generate good quality DOMs and is more important to adapt the number of photos to the scope of the study.

Geo-referencing DOMs is critical for correct orientation measurements. This study show that the outcrop size and its 3D exposure determine whether geo-referencing with ground control points is required or positioning through camera positions is adequate. A correctly georeferenced high-quality model offers brilliant opportunities for orientation measurements and studies that would potentially be very

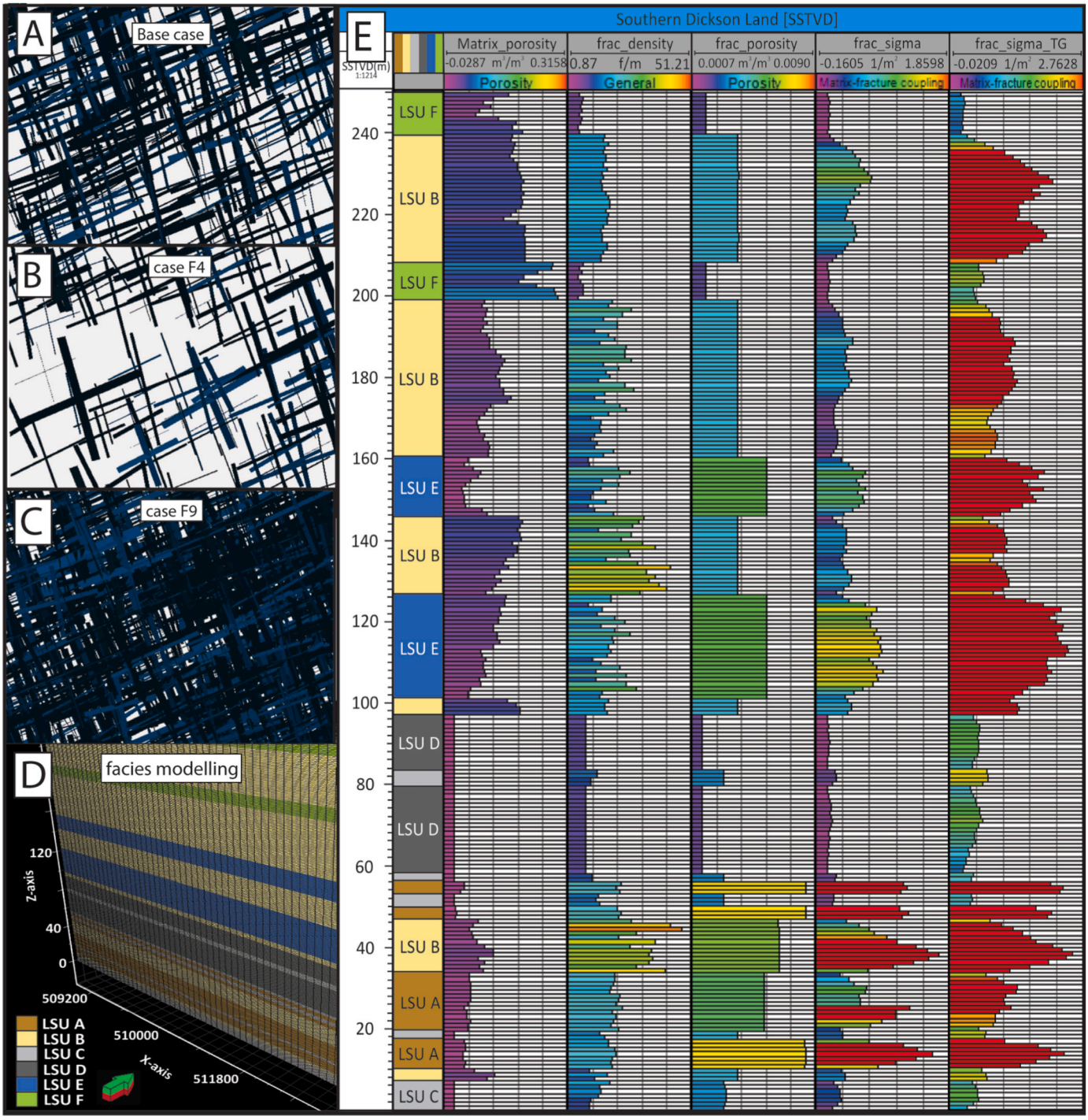

Fig. 11. A)-C) Examples of how the fracture configuration changes in the different cases with different fracture density. All cases are specified in Fig. 12. Fractures are represented as rectangles in the fracture model. D) Facies modelling of the 2.5 × 2.5 × 0.245 km model showing layer-cake indicator krigging based on the LSUs. Vertical exaggeration of 10. E) Summary of selected well data that shows how the data is varying within the logged section. The data is based on input from fieldwork data or output data from the discrete fracture network modelling. Note that frac_sigma (fracture connectivity) is divided into two different results. The column furthest to the right shows frac_sigma and includes the through-going fracture sets interpreted from Esperantodalen and Skansen (location in Fig. 1).

time-consuming or impossible to conduct through traditional fieldwork. DOMs can reveal structures (i.e. 3D structures, faults, fractures) that are difficult to observe from ground or regular fieldwork (Agar and Geiger, 2015). The use of DOMs could potentially bridge the gap between seismic and well data, thereby contributing to an increased understanding of geological 3D geometries in the subsurface (Enge et al., 2007).

As shown, DOMs can be analyzed using manual (LIME) and automatic (PlaneDetect) mapping methods. With these methods we obtained 7269 fracture measurements from DOMs. The results of the automatic mapping showed that the majority of fracture planes measured on virtual outcrops are oriented parallel to the outcrop orientation, opposite to measurements during fieldwork that are generally oriented perpendicular (Festøy, 2017; Senger et al., 2015a). They attribute a better representation of the true plane orientations to automated fracture mapping due to a lower measuring bias. To

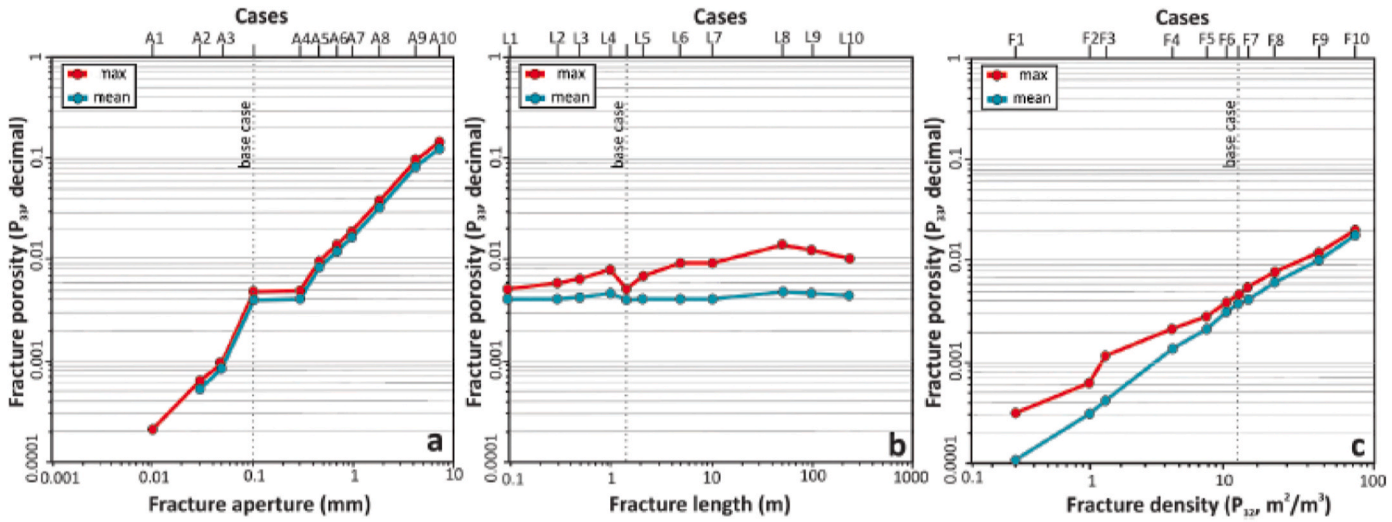

	Fracture aperture		Fracture porosity	
Case	*Mean*	*Max*	*Mean*	*Max*
A1	0.01	-	-	0.0002
A2	0.03	0.03	0.0006	0.0005
A3	0.05	0.05	0.0008	0.0009
Base case	0.1	0.1	0.004	0.0045
A4	0.3	0.3	0.004	0.0045
A5	0.5	0.5	0.008	0.009
A6	0.7	0.7	0.012	0.014
A7	1	1	0.017	0.02
A8	2	2	0.03	0.04
A9	5	5	0.08	0.1
A10	10	10	0.11	0.15

	Fracture aperture		Fracture porosity	
Case	*Mean*	*Max*	*Mean*	*max*
L1	0.1	0.1	0.004	0.005
L2	0.3	0.3	0.004	0.005
L3	0.5	0.5	0.0042	0.0055
L4	1	1	0.0045	0.007
Base case	1.5	1.5	0.004	0.005
L5	2	2	0.004	0.006
L6	5	5	0.004	0.009
L7	10	10	0.004	0.009
L8	50	50	0.005	0.015
L9	100	100	0.0045	0.012
L10	200	200	0.0042	0.01

	Fracture aperture		Fracture porosity	
Case	*Mean*	*Max*	*Mean*	*Max*
F1	0.3	0.3	0.0001	0.0003
F2	1	1	0.0003	0.0006
F3	1.5	1.5	0.0004	0.0015
F4	5	5	0.0017	0.0021
F5	8	8	0.0021	0.0029
F6	10	10	0.003	0.004
Base case	15	15	0.0035	0.0045
F7	20	20	0.004	0.0055
F8	25	25	0.006	0.0075
F9	50	50	0.01	0.015
F10	75	75	0.019	0.02

Fig. 12. Plots showing the relation between fracture porosity (P_{33}) and other parameters; (a) fracture aperture, (b) fracture length and (c) fracture density. Each case is modelled using a 50 × 50 × 50 m synthetic model with a total of 125 000 1 × 1x1 m grid cells. Minimum values of fracture porosity are not plotted since they are assumed to be zero for all cases. All case inputs are listed in the respective tables.

minimize the measuring bias in our field data the window sampling method (Watkins et al., 2015), using the Fieldmove Clino app on an iPhone, was preferred for planes in this study. Therefore, the dataset from the field contains more outcrop-parallel data than using the scan-line method only.

Like traditional field methods, digital photogrammetry is affected by biases and limitations, such as unsatisfying resolution due to distance limitations and outcrops being invisible to the camera. However, the structural rock analyses acquired with traditional fieldwork techniques that can be limited by inaccessible outcrops and steep areas with unfavorable orientations, can be accessed easier with the use of structural analyses on DOMs. Accessing digital photos for DOMs is considered especially useful in areas like Svalbard where the field season is limited due to snow. Harsh arctic conditions and remote locations require high logistical costs, and therefore the advantages of digital geology are high due to the possibility of "re-visiting" the outcrop after fieldwork. A DOM provides the possibility to visualize and interpret the outcrop following fieldwork. This study used digital outcrop in combination with fieldwork to strengthen the dataset and the quantify or the robustness of the data would not be as large without the use of structural measurements from DOMs.

5.3. From outcrop to geo-model

The heterogeneity of the fracture network in a fractured carbonate reservoir is highly dependent on primary (stratigraphical) and secondary (structural and diagenetic) reservoir heterogeneities. Subsurface data (i.e. well and core data, seismic) generally have too low resolution to capture the detailed and spatial irregularity of such complex fracture networks. It is therefore insufficient for proper fracture characterization and geological modelling of heterogeneous carbonate reservoirs (e.g., Casini et al., 2016). Hence, outcrop studies offer an excellent data source to obtain the properties of a fracture network and its heterogeneity. The use of outcrops provides information on geometry and frequencies that is reduced in subsurface data (Fig. 13). It is especially useful to understand fracture formation, classification of fracture sets and their relative spatial distribution (e.g., Wennberg et al., 2016). Fracture parameters from field outcrops can further be used to improve not only fracture estimates in the subsurface, but also extensive reservoir models. Outcrop analogues and fieldwork are an important part of studies related to petroleum systems (Bowman et al., 2016) and have contributed to an improved understanding of subsurface reservoirs (Fig. 13). The use of digital outcrop data provides a larger georeferenced database of fracture characteristics and fracture geometry in a potential subsurface reservoir but will not provide any data on aperture or fluid flow (Bisdom et al., 2016). In contrast to other studies, the modelling workflow in this study is based on outcropping fracture networks characterized from both fieldwork and 3D digital outcrops, as input for stochastic geo-models (Fig. 11). Aperture measured in the field is an unreliable parameter that cannot be properly quantified from outcrop data (Ogata et al., 2014) due to altered outcrop conditions from weathering processes (i.e. frost-weathering, chemical weathering, etc.). These assumptions are supported by the recent study by Van Stappen et al. (2018), who used CT-scanning to investigate the aperture of sandstones in the De Geerdalen Formation as a part of the LYBCO2 project (Braathen et al., 2012; Olaussen et al., 2019; Senger et al., 2015b). The study shows that the rocks exposed in field generally show a larger aperture compared to fractures situated deeper. Fractures situated deeper with increased confining pressure tend to be partly closed with apertures decreasing up to 40% of their original size (Van Stappen et al., 2018). Accurate aperture distribution models for outcropping fractures are challenging to construct and the aperture is recognized to change with fracture spacing, *in situ* loading and the mechanical properties of the rock (Bai et al., 2000). It is common to only consider the effect of the mechanical rock properties and the *in situ* loading (National Research Council, 1996) and therefore assume a constant aperture for all fractures in the total area of

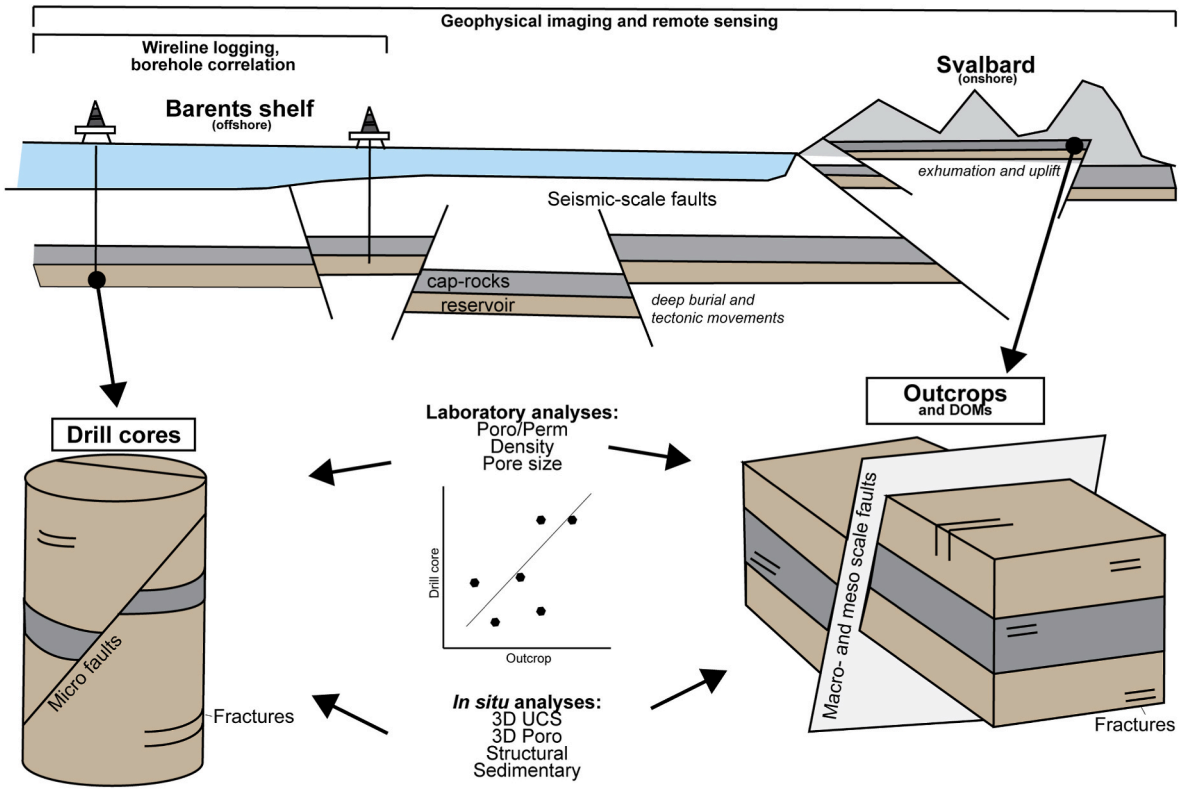

Fig. 13. Synthesis figure illustrating the relationship between the data from offshore (Barents Shelf) and onshore (Svalbard) to better constrain the link. As shown, data from outcrops onshore Svalbard could potentially be used as direct input for bridging gaps to subsurface data from the Barents Shelf such as drill cores and wireline logs. The figure also illustrates the different scales, from geophysical imaging and remote sensing to small scale analyses done in laboratories. UCS = Uniaxial compressive strength. Modified after Kei Ogata.

interest regardless of the fracture spacing (e.g., Bai and Pollard, 2001; Barton et al., 1995).

In this study, data acquired from outcrops in the field are used as input for both digital outcrop modelling and the geological modelling in Petrel. In addition, analyses from the digital outcrop models have contributed to a bigger dataset that could be incorporated into the development of the fracture modelling. Photogrammetry provides efficient generation of models that can be used to acquire data for modelling (Hodgetts, 2013). Digital outcrop modelling presents the opportunity to study and understand the relative impact of multi-scale geological features (e.g., faults, fractures) on reservoir analogues (Agada et al., 2014; Agada and Geiger, 2013).

Even if the geological history of the Kapp Starostin Formation and the equivalent Røye Formation (offshore) are comparable, the fact that the analogue is situated at the surface will present a major difference (Fig. 13). Changes in stress conditions related to the rise of the onshore sequences from a reservoir level and up into the surface, lead to great changes in the characteristics of the fracture network (Mäkel, 2007). It is important to compare all aspects of the geological history and considerate depth changes before outcrop data can fill gaps in subsurface data (Fig. 13) (Cacas et al., 2001). By combining both digital and traditional outcrop studies with DFN modelling, a more advanced and sophisticated approach for the characterization of fracture networks can be established (e.g., Larsen, 2010).

5.3.1. *Outcrop data as input to geomodelling*

The use of outcrop data as direct input in a geological grid model always involves issues regarding scales (Gilman, 2003; Pickup and Hern, 2002). Outcrop heterogeneities are usually measured at smaller scales (i.e. centimeter to meter), whereas grid dimensions and upscaled fracture properties in the models are normally represented in larger scales (i.e. meters to kilometers). Quantifying and integrating the different matrix pore structures and their accompanying deformation structures in a way that gives reasonable illustrations on their impact on reservoir scale is a key challenge when modelling. In this study, the model is incorporated with fracture data on different scales. The outcrops illustrate multiple different heterogeneities that were modelled within the grid cells of the geological model. Beds (layering) and fracture shape were kept constant, whereas the fractures exhibited a large variety of sizes. Typically, a rock volume equivalent to a grid cell in a stochastic model covers two levels of heterogeneity (Pickup and Hern, 2002). Regarding fractures in this study, those heterogeneities are fractures on a bed-confining (BC) scale and a through-going (TG) scale. The BC fractures are modelled with 1–50 m, whereas the large TG fractures exhibit varying lengths up to the vertical limit of the model (i.e. 245 m). However, to avoid computational challenges, the lengths of smaller fractures were adjusted (increased) compared to the field observations. Fractures in field were observed to be on centimeter scale but were kept around 0.5–1.5 m in the 2500 × 2500 × 0.245 m grid model. Fractures normally show a multiscale nature with fracture lengths extending from cm to several km (Wennberg et al., 2016). These lengths are often scale restricted because they are "stratabound" fractures (Odling et al., 1999). A representative expression of the fracture network geometry and permeability on a reservoir simulation grid scale is commonly achieved by using upscaling methods based on the geological scale, i.e. the hydraulic and geometric characteristics of the fracture network (Bourbiaux et al., 1999). These geological scale fracture characteristics are normally measured on a meter scale or smaller, whereas the grid dimensions for field-scale models or reservoir models are tens of meters or larger (Mäkel, 2007). The incorporation of the fracture network from outcrop observations to a grid model presents challenges in terms of the small-scale quantities (Gilman, 2003). This results in a simplified representation reservoir model of the authentic fractured reservoir (e.g., Gorell and Bassett, 2001). Upscaling consequences need to be properly addressed in order

to illustrate the detailed geology sufficiently. It is highly beneficial that model dimensions, interconnection of the network, and flow interactions between the matrix and the fractures are captured in a suitable scale (Mäkel, 2007). A typical mid-sized oil field is between 2 and 20 km^2 in size, with several wells spaced more than hundred meters apart. The size of a geo-model generally spans only hundreds of meters or few kilometers. There is a limited number of outcrops that are large enough to be suitable to understand reservoir geometries at a field scale (Howell et al., 2014).

5.3.2. Sources of error and uncertainty

A geological model is generally built from both subjective interpretation of data and mathematical interpolation/extrapolation techniques. Therefore, the model contains uncertainties. The sources of error can be connected to data acquisition, the input parameters or the process of geological modelling.

There are always some errors tied to the data acquisition in the field. Often acquisition of outcrop data provide uncertainties in the dataset by several factors; (i) the natural variability is not properly captured, (ii) the accuracy of the data, and/or (iii) the representativeness of measurements is variable and insufficient (e.g., Martinius and Næss, 2005). Errors and uncertainties caused by sampling biases when measuring fractures in this study were considered, such as uneven fracture surfaces, poor measuring or magnetic field disturbances. The outcrop quality was of poor quality in some places due to weathering and steepness and this might have affected the measured data. A combination of limited time, challenging weather conditions and steep terrain limits the length of scanlines and number of measurements. Santos et al. (2017) summarized the factors that could generate potential uncertainties in data from fieldwork; (a) subjective uncertainties during data acquisition, (b) naturally prone uncertainties, generated by fracture clustering or diagenetic effects on the fracture system, and (3) intrinsic uncertainties generated by the tools used for the measuring. This is also supported by Howell et al. (2014) that stated that the knowledge of potential sampling errors that can bias the outcrop measurements, is fundamental if invalid conclusions are to be avoided from results or subsequent implementation of the data in modelling workflows. The scale differences of the fractures collected in traditional scanlines and virtual scanlines provide a source of error. The fractures are measured to be significantly shorter in scanlines conducted in field compared to the fractures interpreted from virtual scanlines (Appendix B).

Stochastic modelling, as performed in this study, provides number of uncertainties related to the model generated. The model outcome needs to be adapted to hard facts which in turn also includes some uncertainties. In this study, these uncertainties are thought to mainly be related to the input data. Factors such as data acquisition problems, quality checking, scale issues etc., could have affected the input data before implementing it into the model. The model setup usually requires some assumptions, e.g., facies or petrophysical property distributions. Commonly, those assumptions have significant uncertainties attached to them. The dataset for petrophysical modelling in this study is very sparse as there are only ten thin sections which limits the validity of the model. A larger dataset would be required to reduce the uncertainty of the data. It is also important to note that geological models are complex mathematical functions with nonunique solutions, and no model is ever 100% correct. It is therefore critical to use multiple models and realizations, as results from a single model will always deviate from the reality. The uncertainty of the model is reflected by a suite of realizations, meaning that the spread of the realization outcomes highlights a larger uncertainty of the input parameters. A crucial part of stochastic reservoir modelling and fluid flow simulation studies is reduction and uncertainty analyses. Geological uncertainty assessment through analysis of multiple stochastic model realizations for the different input parameter values that are used are under-estimating and do not properly represent the full range of geological uncertainties (e.g., Senger et al., 2015b; Svanes et al., 1994). This is because the errors and uncertainties related to outcrop data are not considered (Martinius and Næss, 2005). Additionally, the nature and relative significance of uncertainty are linked to the nature of the parameter calculated (Massonnat, 2000). Using outcrop data as input for models requires caution due to rock alternations during exhumation and weathering. Especially weathering and diagenesis are critical factors in carbonates as they might influence the rock properties and fracture networks significantly.

5.4. Modelling of a potential carbonate reservoir analogue: implications for reservoir properties

This study includes modelling of a DFN by statistical sampling with a multi-scale approach, analyzing the highly fractured carbonate succession of the Kapp Starostin Formation, which represent a good outcrop analogue for the offshore carbonate play models in the Barents Sea, developed by The Norwegian Petroleum Directorate (NPD). NPD has developed several exploration models for the Mid-Upper Permian carbonate rocks in the Barents Sea (NPD, 2014). Three exploration models are based on carbonates in the Tempelfjorden Group (Fig. 2). The rather recent Neiden (well 7220/6-2 R), Alta (well 7120/11–1) and Gohta (well 7120/1–3) discoveries by Lundin Norway AS on the Loppa High (Fig. 2) confirmed that the late Paleozoic rocks might have significant reservoir potential in the Barents Sea.

The input parameters used for the modelling in this study are retrieved from rocks that are situated several kilometers higher up than the location of a potential reservoir and therefore includes a great amount of uncertainty. Rock properties on outcrop surfaces, such as fracture length, aperture, geometry etc., might not be the same as in the subsurface (Fig. 13). This is an important consideration that need to be taken in account when using outcrop analogues for modelling. However, a realistic DFN model is expected to be a sufficient and good way to display and highlight the potentials of a fractured reservoir analogue (Agada and Geiger, 2013; Agosta et al., 2010; Hardebol et al., 2015). In this study, the model is incorporated with data on different scales and the outcrops illustrate multiple different heterogeneities (Fig. 13).

5.4.1. Reservoir potential of the Kapp Starostin Formation

By linking the modelling results of this study back to the geology it was possible to identify the Kapp Starostin Formation as a potential unconventional reservoir. Based on results from the geological modelling the uppermost parts of the Kapp Starostin Formation could exhibit good reservoir quality, both in terms of the fracture system, but also considering the facies distribution. According to Stemmerik et al. (1999), the carbonates of the Tempelfjorden Group are commonly tight and highly silicified with low reservoir potentials and the authors state that the carbonates might therefore work as regional seals instead. However, this study experienced that the uppermost part of the formation mainly comprises strata with higher porosities and larger spiculites that may represent good reservoir potential. These results are in accordance with the results by Ehrenberg et al. (2001) from the same area (Esperantodalen) that recorded porosities up to 25% in the light spiculitic rocks. The porosity of the light spiculites consists of unfilled interparticle pores such as pores without silicified matrix and/or cement, and open diagenetic fractures (Ehrenberg et al., 2001). High porosities have also been recorded in spiculitic strata on the Finnmark Platform on the Barents shelf (wells 7128/4–1 and 7128/6–1; Ehrenberg et al., 1998). The dense fracture system recorded in parts of the Kapp Starostin Formation (Figs. 11 and 12) is assumed to be well connected and act as conduits between the porous parts of the heterogenous matrix). Parts of the Kapp Starostin Formation could therefore be interpreted as a type I or II reservoir (i.e. Allan and Sun, 2003; Mäkel, 2007; Nelson, 2001) where the porosity and permeability is fully or partly supported by fractures. Based on this assumption and the results from discrete fracture network modelling, the uppermost parts of the Kapp Starostin Formation might represent an unconventional reservoir.

5.5. Applications and implications of workflow

The presented workflow (Fig. 4) results in a static geological model of a carbonate-dominated naturally fractured succession in central Spitsbergen. In essence, the model has all the characteristics in place for future applications, notable fluid flow simulations. These could, for instance, be used to provide insights into likely carrier beds/fracture systems, or likely fluid flow baffles and barriers that need to be considered when producing from analogous reservoirs. Given the large uncertainties on reservoir conditions, fluid phase and the inability to calibrate such simulation models with real production data, we have not conducted this natural step in our study.

This study focuses on the integration of traditional and digital outcrop data into a geological model, with the emphasis on characterizing the natural fracture network in the Kapp Starostin Formation. The model is prepared for further work in order to develop a better understanding of the reservoir quality in the formation as an analogue for a fractured carbonate reservoir. As with any other data-based geo-model, there are opportunities for improvement by including supplementary data sets, examples are; (1) detailed sedimentological analysis to understand the petrophysical properties of the matrix, (2) sedimentary facies and their spatial extent as input for object-based facies modelling (3) incorporation of structural heterogeneities (e.g., sub-seismic faults), to improve the overall structure of the model, (4) poro-perm measurements from plugs to better constrain the matrix properties, (5) analysis of fracture aperture.

In addition, the detailed model can be populated with lithology-based elastic parameters, and serve as input for synthetic seismic modelling (Anell et al., 2016; Lubrano-Lavadera et al., 2019; Rabbel et al., 2018).

6. Conclusion

In this work we have presented a full workflow from field-based data collection, through digital outcrop characterization to the construction of a geology-based model. The approach is especially useful in areas where traditional field methods are constrained by challenging terrain.

We have applied the workflow on an Upper Permian carbonate-dominated succession in Svalbard, focusing on fracture characterization. The workflow integrates multi-scale outcrop data from fieldwork and digital outcrops in a geological model in order to investigate the natural fracture network in the Kapp Starostin Formation and its unconventional reservoir potential. The discrete fracture network is modelled using outcrop data from fieldwork and digital outcrops as stochastic input. Exploiting observations and data from outcrops clearly offer a better understanding of the heterogeneity of the fracture characteristics in a subsurface reservoir. We conclude that emerging tools, in particular digital outcrop models, provide unprecedented means of gathering relevant quantitative data for geomodelling. The use of digital geology has strengthened the dataset in this study significantly.

Sensitivity tests were conducted in order to study the impact of different fracture parameters on the fracture porosity. Parameters such as fracture aperture, fracture density and fracture lengths were changed and analyzed. The results suggest that fracture porosity is highly sensitive to changes in fracture aperture and fracture density, whereas the fracture length has no significant impact.

CRediT authorship contribution statement

Kristine Larssen: Conceptualization, Methodology, Investigation, Resources, Writing - original draft, Visualization, Supervision, Writing - review & editing. **Kim Senger:** Conceptualization, Methodology, Validation, Resources, Writing - original draft, Funding acquisition, Writing - review & editing. **Sten-Andreas Grundvåg:** Validation, Resources, Writing - original draft, Funding acquisition.

Declaration of competing interest

The authors declare that they have no known competing financial interests or personal relationships that could have appeared to influence the work reported in this paper.

Acknowledgements

The present study was funded by the ARCEx project (Research Centre for Arctic Petroleum Exploration) which is funded by the Research Council of Norway (grant number 228107) and industry partners. Schlumberger provided academic licenses for Petrel. We highly appreciate the field assistants for fruitful discussions and good company; Niklas Schaaf, Tom Birchall and Hilde Marita Haraldsvik. An anonymous reviewer and Jan Tveranger are kindly thanked for their suggestions and comments which greatly improved the quality and clarity of the manuscript.

Appendix A. Sedimentary facies descriptions

Table 6
Facies description and interpretation

Facies unit	Description	Stratigraphic interpretation
A	**Brachiopod limestone:** The moderately silicified unit has a grey color with yellow patches of weathering. Float- to rudstone with fine sand/silty matrix. Beds with erosive contacts and a thickness from 10 to 70 cm. Some beds show planar lamination towards the top. Abundant number of brachiopods and shell fragments of varying size from 0.5 cm up to 4 cm (Fig. 6D). The unit has a sharp boundary to the underlying dolostones.	The facies is measured to be around 6.5 m in the study area and interpreted to represent the brachiopod limestone of the Vøringen Member situated above the Gipshuken Formation. This interpretation is supported by Blomeier et al. (2011) and Blomeier et al. (2013) that described the Vøringen Member as a partly silicified brachiopod rich limestone with lesser amounts of other fossils.
B	**Light spiculitic rocks:** Massive yellowish rock unit, abundant with more rigid dark grey elongated chert nodules (Fig. 6C). Fresh fractures are light grey, and small calcite veins are common. The beds show a discontinuous and wavy structure that gives a nodular appearance. The thickness of the nodular formed beds varies from 10 to 50 cm and are often draped by 0.5–1 cm thin layers of black shales. The unit is highly silicified.	Based on the nodular appearance and chert content, this facies is interpreted to be light-colored spiculite rocks (e.g., Blomeier et al., 2013; Ehrenberg et al., 2001).
C	**Dark spiculitic rocks:** Highly silicified dark grey to black spiculitic rocks with thin wavy bedding and drapes of thin black shale layers (Fig. 6B). It is hard to distinguish individual beds, as they are discontinuous and fractured along the	The facies is in general more massive with a darker color than unit B and is therefore interpreted as dark spiculite rocks (Blomeier et al., 2013; Ehrenberg et al., 2001; Matysik et al., 2018).

(*continued on next page*)

Table 6 (*continued*)

Facies unit	Description	Stratigraphic interpretation
	nodular and undulating shape. However, bed thicknesses seemed to range between 1 cm and 35 cm. Nodular concretions of dark grey to black, highly silicified chert dominates. The unit shows bioturbation and small unspecified fossil fragments.	
D	**Brownish limestone:** Grey to dark brownish limestone layers approx. 30 cm thick, with smaller patches of yellow-brown weathering. The unit seems micritic and no clear grains were observed. It is more rigid than the surrounding units and the boundaries to the overlying and underlying units are sharp. Limited amounts of fossils or fossil fragments.	The facies is interpreted to represent a rigid, micritic and silicified brownish limestone with reduced fossil content. Ehrenberg et al. (2001) described a silty argillaceous lime mudstone that shows similarities to this facies.
E	**Alternating light and dark spiculitic rocks:** Cliffs with alternating light and dark spiculitic rocks with gradual boundaries. The layers are between 10 and 90 cm thick, and the bed thickness seems to increase upwards. Some layers are draped with 1–3 cm thick black shale lamina. The whole unit is highly silicified and show similar fracturing along the discontinuous and nodular bedding as observed from other spiculitic rocks (Fig. 6E).	The facies shows a mixed assemblage of facies B and C with generally thicker layers. The two units interfinger and blend into each other. Based on this, the facies is interpreted as alternating light and dark spiculites.
F	**Bryozoan dominated wacke- to packstone:** The unit shows medium to dark grey limestone with yellow patches of weathering. The limestone contains high numbers of bryozoans, with minor brachiopods, and the carbonate can be classified as a wacke- to packstone. White veins dominate through the whole unit.	Based on its high content of bryozoans, the facies is interpreted to represent a bryozoan dominated wacke- to packstone. Limestones rich in bryozoan fragments have also been described by several other authors (Blomeier et al., 2013; Ehrenberg et al., 2001; Ezaki et al., 1994)
G	**Black shales:** Thick unit with laminated dark grey to black shale, dominated by silica sponges. The shale consists mainly of mudstones. Whole sponges and minor unknown fossils can be observed. The unit is less fractured than the spiculitic rocks but shows long through-going fractures that cut through the whole unit and adjacent units.	Due to the dark color and high occurrence of shaley mudstone, the facies is interpreted to represent black shales. The unit has been described by other authors as thinner beds or laminated horizons (i.e. Blomeier et al., 2013).
H	**Massive float-rudstone:** A brown-blackish massive carbonate unit with burrows, echinoderm, bryozoan and brachiopods. The rock can be classified as a floatstone-rudstone with a mud-supported fabric and shows thin, well-stratified bedding. Weathered areas show a light-yellow color. The unit is partly silicified.	The facies is termed a massive floatstone-rudstone due to its massive appearance. The high content of echinoderm fragments may indicate an echinoderm-dominated limestone, as described and classified by Ezaki et al. (1994) and Blomeier et al. (2013).
I	**Blueish chert breccia:** Dark grey angular chert nodules in a massive blueish crystalline quartz cement. The unit is highly silicified and dominated by a messy pattern of calcite and quartz veins. Nodules of dark and light spiculites are common. It is extremely fractured with irregular fracture surfaces. Commonly associated with light spiculites.	Based on the rock appearance and the presence of light spiculites, the rock is interpreted to represent a massive blueish chert breccia. It formed as result of brecciation of the light spiculites. The brecciation may be a result of diagenetic processes such as dissolution, leading to collapse of the light spiculites (e.g., Matysik et al., 2018).
J	**White chert breccia:** The unit is like unit I, but this unit is gradually getting whiter and less rigid. Contains burrows and small fractured silica sponges (Fig. 6A). The chert nodules in the unit are formed along bedding. Quartz veins are dominating. Highly fractured. Several fracture planes are full of precipitated calcite.	This facies is also interpreted to be a chert breccia resulted from diagenetic processes. However, the unit is dominated by crystalline quartz in thick filled vugs and veins.
K	**Glauconitic sandstone:** The unit consists of thicker beds of fine to medium-grained glauconitic sandstone with a distinct pale green color. The unit can be divided into three different sections with slightly different features. The lowermost part contains conjugate fractures, some trace fossils and thinner shale layers. The middle part has thick, cross-stratified beds with angular clasts towards the boundary of the lower part. The upper part is laminated and is intensely fractures compared to the other parts of the unit. The sandstones are well-sorted, moderately bioturbated and partly contain fractured brachiopod shells. The unit is not silicified and is found in close association with light spiculitic rocks.	Based on the sections dominated by fin to medium-grained sandstones with a high content of glauconite, the facies is interpreted to represent the glauconitic sandstones present in the upper parts of the Kapp Starostin Formation, possibly as a part of the Stensiöfjellet Member (e.g., Ehrenberg et al., 2001b; Ezaki et al., 1994).
L	**Silicified glauconitic sandstone:** Glauconitic sandstone unit that is highly silicified. The sandstone is fine-grained with smaller transported clasts of shale some places. Planar-parallel lamination can be observed some in places. The unit can be divided into two parts where the upper most part is more resistant and shows less fractures than the lower one. The whole unit is heavily fractured and weathered, making it hard to identify any clear bedding.	An additional facies with glauconitic sandstones. However, this sandstone is highly silicified and are therefore described as a silicified glauconitic sandstone.

Appendix B. Scanlines

Table 7
Overview of all scanlines acquired in this study.

Profile ID	Locality	Locality abbreviation	Lithology	Length (m)	Fractures (n)	Fractures/m (mean)
Scanlines						
KL_1	Idodalen south A	ld_s_a	Brachiopod limestone	1.75	25	14.29
KL_2	Espérant oda len south	E_S	Black shales	4.93	39	7.91
KL_3	Esperant oda len south	E_S	Light spiculites	0.99	31	31.31
KL_4	Idodalen waterfall	ld_w	Brachiopod limestone	2.96	57	19.26
KL_5	Idodalen waterfall	ld_w	Light spiculites	1.00	38	38
KL_6	Idodalen south c	ld_s_c	Light spiculites	2.00	95	47.50
KL_7	Espérant oda len south	E_S	Brownish limestone	2.32	74	31.90
Total				**15.95**	**359**	
Virtual profiles						
Ef_1	Eskerfossen north	Ef_N	Light spiculites	1.26	24	19.05
Ef_2	Eskerfossen north	Ef_N	Light spiculites	2.57	34	13.23
Ef_3	Eskerfossen north	Ef_N	Light spiculites	2.4	37	15.42
Ef_4	Eskerfossen north	Ef_N	Light spiculites	2.32	45	19.40

(*continued on next page*)

Table 7 (*continued*)

Profile ID	Locality	Locality abbreviation	Lithology	Length (m)	Fractures (n)	Fractures/m (mean)
Ef_5	Eskerfossen north	Ef_N	Light spiculites	2.34	46	19.66
E_N_1	Esperantodalen north	E_N	Mixed	283.91	47	0.17
E_N_2	Esperantodalen north	E_N	Mixed	315.87	66	0.21
E_N_3	Esperantodalen north	E_N	Mixed	311.30	31	0.10
E_N_4	Esperantodalen north	E_N	Mixed	328.26	25	0.08
E_N_5	Esperantodalen north	E_N	Mixed	345.44	24	0.07
E_S_1	Esperantodalen south	E_S	Mixed	212.85	24	0.11
E_S_2	Esperantodalen south	E_S	Mixed	212.57	42	0.20
E_S_3	Esperantodalen south	E_S	Mixed	218.14	38	0.17
E_S_4	Esperantodalen south	E_S	Mixed	228.28	38	0.17
E_S_5	Esperantodalen south	E_S	Mixed	207.37	33	0.16
Hf_1	Heimenfjellet	Hf	Light spiculites	2.4	35	14.58
Hf_2	Heimenfjellet	Hf	Light spiculites	2.37	42	17.72
Hf_3	Heimenfjellet	Hf	Light spiculites	2.56	47	18.36
ld_1	Idodalen south B	ld_s_b	Brownish limestone	2.17	32	14.75
ld_2	Idodalen south B	ld_s_b	Brownish limestone	3.27	45	13.76
ld_3	Idodalen south B	ld_s_b	Brownish limestone	3.01	38	12.62
ld_s_d_1	Idodalen south D	ld_s_d	Light spiculites	3.75	36	9.60
ld_s_d_2	Idodalen south D	ld_s_d	Light spiculites	4.09	38	9.29
ld_s_d_3	Idodalen south D	ld_s_d	Light spiculites	4.01	53	13.22
ld_s_d_4	Idodalen south D	ld_s_d	Light spiculites	4.2	52	12.38
ld_s_d_5	Idodalen south D	ld_s_d	Light spiculites	4.51	51	11.31
Total				**2711.22**	**1023**	

References

Agada, S., Chen, F., Geiger, S., Toigulova, G., Agar, S., Shekhar, R., Benson, G., Hehmeyer, O., Amour, F., Mutti, M., 2014. Numerical Simulation of Fluid-Flow Processes in a 3D High-Resolution Carbonate Reservoir Analogue.

Agada, S., Geiger, S., 2013. Optimising gas injection in carbonate reservoirs using high-resolution outcrop analogue models. In: SPE Reservoir Characterization and Simulation Conference and Exhibition. Society of Petroleum Engineers.

Agar, S.M., Geiger, S., 2015. Fundamental controls on fluid flow in carbonates: current workflows to emerging technologies. Geological Society, London, Special Publications 406, 1–59.

Agosta, F., Alessandroni, M., Antonellini, M., Tondi, E., Giorgioni, M., 2010. From fractures to flow: a field-based quantitative analysis of an outcropping carbonate reservoir. Tectonophysics 490, 197–213.

Ahlborn, M., Stemmerik, L., Kalstø, T.-K., 2014. 3D seismic analysis of karstified interbedded carbonates and evaporites, lower permian gipsdalen Group, Loppa high, southwestern Barents Sea. Mar. Petrol. Geol. 56, 16–33.

Ahr, W.M., 2011. Geology of Carbonate Reservoirs: the Identification, Description and Characterization of Hydrocarbon Reservoirs in Carbonate Rocks. John Wiley & Sons.

Allan, J., Sun, S.Q., 2003. Controls on recovery factor in fractured reservoirs: lessons learned from 100 fractured fields. In: SPE Annual Technical Conference and Exhibition. Society of Petroleum Engineers.

Anell, I., Lecomte, I., Braathen, A., Buckley, S., 2016. Synthetic seismic illumination of small-scale growth faults, paralic deposits and low-angle clinoforms: a case study of the Triassic successions on Edgeøya, NW Barents Shelf. Mar. Petrol. Geol. 77, 625–639.

Bai, T., Pollard, D.D., 2001. Getting more for less: the unusual efficiency of fluid flow in fractures. Geophys. Res. Lett. 28, 65–68.

Bai, T., Pollard, D.D., Gross, M.R., 2000. Mechanical prediction of fracture aperture in layered rocks. J. Geophys. Res.: Solid Earth 105, 707–721.

Barton, C.A., Zoback, M.D., Moos, D., 1995. Fluid flow along potentially active faults in crystalline rock. Geology 23, 683–686.

Belayneh, M.W., Matthai, S.K., Blunt, M.J., Rogers, S.F., 2009. Comparison of deterministic with stochastic fracture models in water-flooding numerical simulations. AAPG Bull. 93, 1633–1648.

Bergh, S.G., Braathen, A., Andresen, A., 1997. Interaction of basement-involved and thin-skinned tectonism in the Tertiary fold-thrust belt of central Spitsbergen, Svalbard. AAPG (Am. Assoc. Pet. Geol.) Bull. 81, 637–661.

Bisdom, K., Bertotti, G., Nick, H.M., 2016. The impact of in-situ stress and outcrop-based fracture geometry on hydraulic aperture and upscaled permeability in fractured reservoirs. Tectonophysics 690, 63–75.

Bisdom, K., Nick, H., Bertotti, G., 2017. An integrated workflow for stress and flow modelling using outcrop-derived discrete fracture networks. Comput. Geosci. 103, 21–35.

Bjorlykke, K., 1984. Formation of Secondary Porosity: How Important Is it?: Part 2. Aspects of Porosity Modification.

Blomeier, D., Dustira, A., Forke, H., Scheibner, C., 2011. Environmental change in the early permian of NE svalbard: from a warm-water carbonate platform (gipshuken formation) to a temperate, mixed siliciclastic-carbonate ramp (Kapp Starostin Formation). Facies 57, 493–523.

Blomeier, D., Dustira, A.M., Forke, H., Scheibner, C., 2013. Facies analysis and depositional environments of a storm-dominated, temperate to cold, mixed siliceous-carbonate ramp: the Permian Kapp Starostin Formation in NE Svalbard. Norwegian Journal of Geology/Norsk Geologisk Forening 93, 75–93.

Blomeier, D., Scheibner, C., Forke, H., 2009. Facies arrangement and cyclostratigraphic architecture of a shallow-marine, warm-water carbonate platform: the late carboniferous ny friesland platform in eastern spitsbergen (pyefjellet beds, wordiekammen formation, gipsdalen Group). Facies 55, 291–324.

Bond, D.P., Blomeier, D., Dustira, A., Wignall, P., Collins, D., Goode, T., Groen, R., Buggisch, W., Grasby, S., 2017. Sequence stratigraphy, basin morphology and Sea-level history for the permian Kapp Starostin Formation of svalbard, Norway. Geological Magazine, pp. 1–17.

Boro, H., Rosero, E., Bertotti, G., 2014. Fracture-network analysis of the Latemar Platform (northern Italy): integrating outcrop studies to constrain the hydraulic properties of fractures in reservoir models. Petrol. Geosci. 20, 79–92.

Bourbiaux, B., Granet, S., Landereau, P., Noetinger, B., Sarda, S., Sabathier, J., 1999. Scaling up Matrix-Fracture Transfers in Dual-Porosity Models: Theory and Application, SPE Annual Technical Conference and Exhibition. Society of Petroleum Engineers.

Bowman, M., Smyth, H.R., Passey, S., Hirst, J., Jordan, C., 2016. The Value of Outcrop Studies in Reducing Subsurface Uncertainty and Risk in Hydrocarbon Exploration and Production. Geological Society of London.

Braathen, A., Bergh, S.G., Maher Jr., H.D., 1999. Application of a critical wedge taper model to the Tertiary transpressional fold-thrust belt on Spitsbergen, Svalbard. Geol. Soc. Am. Bull. 111, 1468–1485.

Braathen, A., Bælum, K., Christiansen, H.H., Dahl, T., Eiken, O., Elvebakk, H., Hansen, F., Hanssen, T.H., Jochmann, M., Johansen, T.A., Johnsen, H., Larsen, L., Lie, T., Mertes, J., Mørk, A., Mørk, M.B., Nemec, W.J., Olaussen, S., Oye, V., Rød, K., Titlestad, G.O., Tveranger, J., Vagle, K., 2012. Longyearbyen CO_2 lab of Svalbard, Norway – first assessment of the sedimentary succession for CO_2 storage. Norw. J. Geol. 92, 353–376.

Buckley, S.J., Howell, J.A., Enge, H.D., Kurz, T.H., 2008. Terrestrial laser scanning in geology: data acquisition, processing and accuracy considerations. J. Geol. Soc. 165, 625–638.

Buckley, S.J., Ringdal, K., Naumann, N., Dolva, B., Kurz, T.H., Howell, J.A., Dewez, T.J., 2019. LIME: software for 3-D visualization, interpretation, and communication of virtual geoscience models. Geosphere 15, 222–235.

Bælum, K., Braathen, A., 2012. Along-strike changes in fault array and rift basin geometry of the Carboniferous Billefjorden Trough, Svalbard, Norway. Tectonophysics 546, 38–55.

Cacas, M., Daniel, J., Letouzey, J., 2001. Nested geological modelling of naturally fractured reservoirs. Petrol. Geosci. 7, S43–S52.

Carrivick, J.L., Smith, M.W., Quincey, D.J., 2016. Structure from Motion in the Geosciences. John Wiley & Sons.

Casini, G., Hunt, D., Monsen, E., Bounaim, A., 2016. Fracture characterization and modeling from virtual outcrops. AAPG (Am. Assoc. Pet. Geol.) Bull. 100, 41–61.

Chesley, J., Leier, A., White, S., Torres, R., 2017. Using unmanned aerial vehicles and structure-from-motion photogrammetry to characterize sedimentary outcrops: an example from the Morrison Formation, Utah, USA. Sediment. Geol. 354, 1–8.

Dallmann, W., 2015. Geoscience atlas of svalbard. Norsk Polarinstitutt Rapportserie 148, 292.

Dallmann, W.K., Andresen, A., Bergh, S., Maher Jr., H.D., Ohta, Y., 1993. Tertiary fold-and-thrust belt of Spitsbergen, Svalbard. (map scale 1:200 000). Nor. Polarinst. Medd. 128, 46.

Davies, R.J., 2005. Differential compaction and subsidence in sedimentary basins due to silica diagenesis: a case study. Geol. Soc. Am. Bull. 117, 1146–1155.

Dershowitz, W.S., Herda, H.H., 1992. Interpretation of fracture spacing and intensity. In: Tillerson, Wawersik (Ed.), Rock Mechanics. Balkerna, Rotterdam, pp. 757–766.

Dimakis, P., Braathen, B.I., Faleide, J.I., Elverhøi, A., Gudlaugsson, S.T., 1998. Cenozoic erosion and the preglacial uplift of the Svalbard–Barents Sea region. Tectonophysics 300, 311–327.
Ding, W., Fan, T., Yu, B., Huang, X., Liu, C., 2012. Ordovician carbonate reservoir fracture characteristics and fracture distribution forecasting in the Tazhong area of Tarim Basin, Northwest China. J. Petrol. Sci. Eng. 86, 62–70.
Dörr, N., Clift, P., Lisker, F., Spiegel, C., 2013. Why is Svalbard an island? Evidence for two-stage uplift, magmatic underplating, and mantle thermal anomalies. Tectonics 32, 473–486.
Døssing, A., Jackson, H.R., Matzka, J., Einarsson, I., Rasmussen, T.M., Olesen, A.V., Brozena, J.M., 2013. On the origin of the amerasia basin and the high arctic large igneous province—results of new aeromagnetic data. Earth Planet Sci. Lett. 363, 219–230.
Ehrenberg, S., Pickard, N., Henriksen, L., Svana, T., Gutteridge, P., Macdonald, D., 2001. A depositional and sequence stratigraphic model for cold-water, spiculitic strata based on the Kapp Starostin Formation (Permian) of Spitsbergen and equivalent deposits from the Barents Sea. AAPG Bull. 85, 2061–2088.
Ehrenberg, S.N., Nielsen, E.B., Svana, T., Stemmerik, L., 1998. Diagenesis and reservoir quality of the Finnmark carbonate platform, Barents Sea: results from wells 7128/6-1 and 7128/4-1. Nor. Geol. Tidsskr. 78, 225–251.
Enge, H.D., Buckley, S.J., Rotevatn, A., Howell, J.A., 2007. From outcrop to reservoir simulation model: workflow and procedures. Geosphere 3, 469–490.
Ezaki, Y., Kawamura, T., Nakamura, K., 1994. Kapp Starostin Formation in Spitsbergen: a Sedimentary and Faunal Record of Late Permian Palaeoenvironments in an Arctic Region.
Faleide, J.I., Gudlaugsson, S.T., Jacquart, G., 1984. Evolution of the western Barents Sea. Mar. Petrol. Geol. 1, 123–150.
Festøy, M., 2017. Integrated Characterization of Igneous Intrusions in Central Spitsbergen. University of Tromsø/UNIS.
Galland, O., Spacapan, J.B., Rabbel, O., Mair, K., Soto, F.G., Eiken, T., Schiuma, M., Leanza, H.A., 2019. Structure, emplacement mechanism and magma-flow significance of igneous fingers – implications for sill emplacement in sedimentary basins. J. Struct. Geol. 124, 120–135.
Gilman, J.R., 2003. Practical Aspects of Simulation of Fractured Reservoirs. International Forum on Reservoir Simulation, Buhl, Baden-Baden, Germany, pp. 23–27.
Gorell, S., Bassett, R., 2001. Trends in reservoir simulation: big models, scalable models? Will you please make up your mind? SPE Annual Technical Conference and Exhibition. Society of Petroleum Engineers.
Gradstein, F.M., Anthonissen, E., Brunstad, H., Charnock, M., Hammer, O., Hellem, T., Lervik, K.S., 2010. Norwegian offshore stratigraphic lexicon (NORLEX). Newsl. Stratigr. 44, 73–86.
Grove, C., Jerram, D.A., 2011. jPOR: an ImageJ macro to quantify total optical porosity from blue-stained thin sections. Comput. Geosci. 37, 1850–1859.
Grundvåg, S., 2008. Facies Analysis, Sequence Stratigraphy and Geochemistry of the Middle-Upper Permian Kapp Starostin Formation, Central Spitsbergen.. Unpublished MSc thesis Department of Geology, University of Tromsø.
Guerriero, V., Mazzoli, S., Iannace, A., Vitale, S., Carravetta, A., Strauss, C., 2013. A permeability model for naturally fractured carbonate reservoirs. Mar. Petrol. Geol. 40, 115–134.
Hardebol, N.J., Maier, C., Nick, H., Geiger, S., Bertotti, G., Boro, H., 2015. Multiscale fracture network characterization and impact on flow: a case study on the Latemar carbonate platform. J. Geophys. Res.: Solid Earth 120, 8197–8222.
Haremo, P., Andresen, A., Dypvik, H., Nagy, J., Elverhøi, A., Eikeland, T.A., Johansen, H., 1990. Structural development along the Billefjorden Fault zone in the area between kjellströmdalen and adventdalen/sassendalen, central spitsbergen. Polar Res. 8, 195–216.
Harland, W.B., 1997. The Geology of Svalbard. Geological Society Memoir Nr. 17 The Geological Society, Bath, United Kingdom, p. 525.
Harland, W.B., Cutbill, J.L., Friend, P.F., Gobbet, D.J., Holliday, D.W., Maton, P.I., Parker, J.R., Wallis, R.H., 1974. The Billefjorden Fault Zone, Spitsbergen, the long history of a major tectonic lineament. Nor. Polarinst. Skr. 161.
Henriksen, E., Ryseth, A.E., Larssen, G.B., Heide, T., Rønning, K., Sollid, K., Stoupakova, A.V., 2011. Chapter 10 Tectonostratigraphy of the greater Barents Sea: implications for petroleum systems. In: Spencer, A.M., Embry, A.F., Gautier, D.L., Stoupakova, A.V., Sørensen, K. (Eds.), Arctic Petroleum Geology. The Geological Society, London, pp. 163–195.
Hodgetts, D., 2013. Laser scanning and digital outcrop geology in the petroleum industry: a review. Mar. Petrol. Geol. 46, 335–354.
Hodgetts, D., Drinkwater, N., Hodgson, J., Kavanagh, J., Flint, S., Keogh, K., Howell, J., 2004. Three-dimensional geological models from outcrop data using digital data collection techniques: an example from the Tanqua Karoo depocentre, South Africa. Geological Society, London, Special Publications 239, 57–75.
Howell, J.A., Martinius, A.W., Good, T.R., 2014. The application of outcrop analogues in geological modelling: a review, present status and future outlook. In: Martinius, A. W., Howell, J.A., Good, T.R. (Eds.), Sediment-Body Geometry and Heterogeneity: Analogue Studies for Modelling the Subsurface. Geological Society of London, London, pp. 1–25.
Hüneke, H., Joachimski, M., Buggisch, W., Lützner, H., 2001. Marine carbonate facies in response to climate and nutrient level: the upper carboniferous and permian of central spitsbergen (svalbard). Facies 45, 93–135.
Johannessen, E.P., Steel, R.J., 1992. Mid-carboniferous extension and rift-infill sequences in the Billefjorden Trough, svalbard. Nor. Geol. Tidsskr. 72, 35–48.
Jones Jr., F.O., 1975. A laboratory study of the effects of confining pressure on fracture flow and storage capacity in carbonate rocks. J. Petrol. Technol. 27, 21–27.
Khoshbakht, F., Azizzadeh, M., Memarian, H., Nourozi, G., Moallemi, S., 2012. Comparison of electrical image log with core in a fractured carbonate reservoir. J. Petrol. Sci. Eng. 86, 289–296.
Kim, T.H., Schechter, D.S., 2009. Estimation of fracture porosity of naturally fractured reservoirs with No matrix porosity using fractal discrete fracture networks. SPE J. 110720, 11.
Kingston, D., Dishroon, C., Williams, P., 1983. Hydrocarbon plays and global basin classification. AAPG Bull. 67, 2194–2198.
Larsen, T., 2010. Fractured Carbonates in the Mediumfjellet Thrust-Stack in the Tertiary Fold-And-Thrust Belt of Spitsbergen. Department of Arctic Geology. University of Tromsø, Tromsø.
Larssen, G.B., Elvebakk, G., Henriksen, L.B., Krsistensen, S.E., Nillson, I., Samuelsberg, T. J., Svånå, T.A., Stemmerik, L., Worsley, D., 2005. Upper palaeozoic lithostratigraphy of the southern part of the Norwegian Barents Sea. NGU-Bulletin 444, 1–43.
Larssen, K., 2018. Integrated Characterization of the Upper Permian Kapp Starostin Formation in Central Spitsbergen, Svalbard. From Outcrop to Geomodel. Department of Geosciences. University of Tromsø, Tromsø, Norway.
Lato, M.J., Vöge, M., 2012. Automated mapping of rock discontinuities in 3D lidar and photogrammetry models. Int. J. Rock Mech. Min. Sci. 54, 150–158.
Lattman, L., Parizek, R.R., 1964. Relationship between fracture traces and the occurrence of ground water in carbonate rocks. J. Hydrol. 2, 73–91.
Leever, K.A., Gabrielsen, R.H., Faleide, J.I., Braathen, A., 2011. A transpressional origin for the West Spitsbergen fold-and-thrust belt: insight from analog modeling. Tectonics 30.
Lerch, B., Karlsen, D.A., Abay, T.B., Duggan, D., Seland, R., Backer-Owe, K., 2016. Regional petroleum alteration trends in Barents Sea oils and condensates as a clue to migration regimes and processes. AAPG (Am. Assoc. Pet. Geol.) Bull. 100, 165–190.
Liu, E., Martinez, A., 2014. Seismic Fracture Characterization. Elsevier.
Loucks, R.G., 1999. Paleocave carbonate reservoirs: origins, burial-depth modifications, spatial complexity, and reservoir implications. AAPG Bull. 83, 1795–1834.
Lubrano-Lavadera, P., Senger, K., Mulrooney, M., Lecomte, I., Kuehn, D., 2019. Synthetic seismic modelling of small-scale faults: implications for CO2 imaging of a High Arctic CO2 storage site. Norw. J. Geol.
Lønøy, A., 2006. Making sense of carbonate pore systems. AAPG Bull. 90, 1381–1405.
Malkowski, K., 1982. Development and stratigraphy of the Kapp Starostin Formation (permian) of spitsbergen. Palaeontol. Pol. 43, 69–81.
Martinius, A., Næss, A., 2005. Uncertainty analysis of fluvial outcrop data for stochastic reservoir modelling. Petrol. Geosci. 11, 203–214.
Massonnat, G., 2000. Can we sample the complete geological uncertainty space in reservoir-modeling uncertainty estimates? SPE J. 5, 46–59.
Matysik, M., Stemmerik, L., Olaussen, S., Brunstad, H., 2018. Diagenesis of spiculites and carbonates in a permian temperate ramp succession–tempelfjorden Group, spitsbergen, arctic Norway. Sedimentology 65, 745–774.
Michelsen, J.K., Khorasani, G.K., 1991. A regional study on coals from Svalbard; organic facies, maturity and thermal history. Bull. Soc. Geol. Fr. 162, 385–397.
Montanari, D., Minissale, A., Doveri, M., Gola, G., Trumpy, E., Santilano, A., Manzella, A., 2017. Geothermal resources within carbonate reservoirs in western Sicily (Italy): a review. Earth Sci. Rev. 169, 180–201.
Mäkel, G., 2007. The modelling of fractured reservoirs: constraints and potential for fracture network geometry and hydraulics analysis. Geological Society, London, Special Publications 292, 375–403.
National Research Council, 1996. Rock Fractures and Fluid Flow: Contemporary Understanding and Applications. National Academies Press.
Nelson, R., 2001. Geologic Analysis of Naturally Fractured Reservoirs. Elsevier.
Nicolaisen, J., Elvebakk, G., Ahokas, J., Bojesen-Koefoed, J., Olaussen, S., Rinna, J., Skeie, J., Stemmerik, L., 2019. Characterization of upper palaeozoic organic-rich units in svalbard: implications for the petroleum systems of the Norwegian Barents shelf. J. Petrol. Geol. 42, 59–78.
NPD, 2014. Barentshavet - Midtre Til Øvre Perm Letemodeller. http://www.npd.no/no/Tema/Geologi/Letemodeller/Barentshavet/Midtre-til-ovre-perm/.
Oda, M., 1985. Permeability tensor for discontinuous rock masses. Geotechnique 35, 483–495.
Odling, N.E., Gillespie, P., Bourgine, B., Castaing, C., Chiles, J.P., Christensen, N.P., Fillion, E., Genter, A., Olsen, C., Thrane, L., Trice, R., Aarseth, E., Walsh, J.J., Watterson, J., 1999. Variations in fracture system geometry and their implications for fluid flow in fractures hydrocarbon reservoirs. Petrol. Geosci. 5, 373–384.
Ogata, K., Senger, K., Braathen, A., Tveranger, J., Olaussen, S., 2014. Fracture systems and meso-scale structural patterns in the siliciclastic Mesozoic reservoir-caprock succession of the Longyearbyen CO2 Lab project: implications for geologic CO2 sequestration on Central Spitsbergen, Svalbard. Norw. J. Geol. 94, 121–154.
Olaussen, S., Senger, K., Braathen, A., Grundvåg, S.-A., Mørk, A., 2019. You learn as long as you drill; research synthesis from the Longyearbyen CO2 Laboratory, Svalbard, Norway. Norw. J. Geol. 99, 157–188.
Ozkaya, S.I., Richard, P.D., 2006. Fractured reservoir characterization using dynamic data in a carbonate field, Oman. SPE Reservoir Eval. Eng. 9, 227–238.
Pérez, M.A., Grechka, V., Michelena, R.J., 1999. Fracture detection in a carbonate reservoir using a variety of seismic methods. Geophysics 64, 1266–1276.
Pickup, G., Hern, C., 2002. The development of appropriate upscaling procedures. Transport Porous Media 46, 119–138.
Polteau, S., Hendriks, B.W., Planke, S., Ganerød, M., Corfu, F., Faleide, J.I., Midtkandal, I., Svensen, H.S., Myklebust, R., 2016. The early cretaceous Barents Sea sill complex: distribution, 40 Ar/39 Ar geochronology, and implications for carbon gas formation. Palaeogeogr. Palaeoclimatol. Palaeoecol. 441, 83–95.
Pringle, J.K., Clark, J.D., Westerman, A.R., Stanbrook, D.A., Gardiner, A.R., Morgan, B., 2001. Virtual outcrops: 3-D reservoir analogues. Animations in Geology. J. Virtual Explor. 3, 00-01.

Pringle, J.K., Howell, J.A., Hodgetts, D., Westerman, A.R., Hodgson, D.M., 2006. Virtual outcrop models of petroleum reservoir analogues: a review of the current state-of-the-art. First Break 24, 33–42.
Rabbel, O., Galland, O., Mair, K., Lecomte, I., Senger, K., Spacapan, J.B., Manceda, R., 2018. From field analogues to realistic seismic modelling: a case study of an oil-producing andesitic sill complex in the Neuquén Basin, Argentina. J. Geol. Soc.
Reijers, T., Bartok, P., 1985. Porosity Characteristics and Evolution in Fractured Cretaceous Carbonate Reservoirs, La Paz Field Area, Maracaibo Basin, Venezuela, Carbonate Petroleum Reservoirs. Springer, pp. 407–423.
Rittersbacher, A., Buckley, S.J., Howell, J.A., Hampson, G.J., Vallet, J., 2013. Helicopter-based laser scanning: a method for quantitative analysis of large-scale sedimentary architecture. In: Martinius, A.W., Howell, J.A., Good, T. (Eds.), Sediment-body Geometry and Heterogeneity: Analogue Studies for Modelling the Subsurface. Geological Society of London Special Publication #387, London, pp. 1–18.
Roehl, P.O., Choquette, P.W., 2012. Carbonate Petroleum Reservoirs. Springer Science & Business Media.
Rohrbaugh Jr., M., Dunne, W., Mauldon, M., 2002. Estimating fracture trace intensity, density, and mean length using circular scan lines and windows. AAPG Bull. 86, 2089–2104.
Santos, S.M., Gaspar, A.T., Schiozer, D.J., 2017. Value of information in reservoir development projects: technical indicators to prioritize uncertainties and information sources. J. Petrol. Sci. Eng. 157, 1179–1191.
Senger, K., Buckley, S.J., Chevallier, L., Fagereng, Å., Galland, O., Kurz, T.H., Ogata, K., Planke, S., Tveranger, J., 2015a. Fracturing of doleritic intrusions and associated contact zones: implications for fluid flow in volcanic basins. J. Afr. Earth Sci. 102, 70–85.
Senger, K., Roy, S., Braathen, A., Buckley, S.J., Bælum, K., Gernigon, L., Mjelde, R., Noormets, R., Ogata, K., Olaussen, S., Planke, S., Ruud, B.O., Tveranger, J., 2013. Geometries of doleritic intrusions in central Spitsbergen, Svalbard: an integrated study of an onshore-offshore magmatic province with implications on CO_2 sequestration. Norw. J. Geol. 93, 143–166.
Senger, K., Tveranger, J., Braathen, A., Olaussen, S., Ogata, K., Larsen, L., 2015b. CO_2 storage resource estimates in unconventional reservoirs: insights from a pilot-sized storage site in Svalbard, Arctic Norway. Environmental Earth Sciences 73, 3987–4009.
Senger, K., Tveranger, J., Ogata, K., Braathen, A., Planke, S., 2014. Late mesozoic magmatism in svalbard: a review. Earth Sci. Rev. 139, 123–144.
Shakiba, M., Ayatollahi, S., Riazi, M., 2016. Investigation of oil recovery and CO2 storage during secondary and tertiary injection of carbonated water in an Iranian carbonate oil reservoir. J. Petrol. Sci. Eng. 137, 134–143.
Singhal, B.B.S., Gupta, R.P., 2010. Hydrogeology of Volcanic Rocks Applied Hydrogeology of Fractured Rocks. Springer Netherlands, pp. 257–268.
Smelror, M., Petrov, O., Larssen, G.B., Werner, S., 2009. Geological history of the Barents Sea. Norges Geol. undersøkelse 1–135.
Smith, M., Carrivick, J., Quincey, D., 2016. Structure from motion photogrammetry in physical geography. Prog. Phys. Geogr. 40, 247–275.
Smyrak-Sikora, A., Johannessen, E.P., Olaussen, S., Sandal, G., Braathen, A., 2019. Sedimentary architecture during Carboniferous rift initiation–the arid Billefjorden Trough, svalbard. J. Geol. Soc. 176, 225–252.
Sorento, T., Olaussen, S., Stemmerik, L., 2020. Controls on deposition of shallow marine carbonates and evaporites–lower Permian Gipshuken Formation, central Spitsbergen, Arctic Norway. Sedimentology 67, 207–238.
Steel, R.J., Worsley, D., 1984. Svalbard's post-Caledonian strata - an atlas of sedimentational patterns and paleogeographic evolution. In: Spencer, A.M. (Ed.), Petroleum Geology of the North European Margin. Graham & Trotman, London, pp. 109–135.
Stemmerik, L., 2000. Late palaeozoic evolution of the north atlantic margin of pangea. Palaeogeogr. Palaeoclimatol. Palaeoecol. 161, 95–126.
Stemmerik, L., Elvebakk, G., Worsley, D., 1999. Upper Palaeozoic carbonate reservoirs on the Norwegian arctic shelf; delineation of reservoir models with application to the Loppa High. Petrol. Geosci. 5, 173–187.
Strand, S.A.H., 2015. Layer Parallel Shortening and Cataclastic Flow by Fractures in the Permian Kapp Starostin Formation, Mediumfjellet, Spitsbergen. The University of Bergen.
Sturzenegger, M., Stead, D., 2009. Quantifying discontinuity orientation and persistence on high mountain rock slopes and large landslides using terrestrial remote sensing techniques. Nat. Hazards Earth Syst. Sci. 9.
Svanes, T., Karstad, P., Myking, B., Hovland, F., Madsen, M., 1994. Detailed Stochastic Modelling of a Proximal Fluvial Reservoir with Realizations Used in Flow Simulation, European Petroleum Conference. Society of Petroleum Engineers.
Talwani, M., Eldholm, O., 1977. Evolution of the Norwegian-Greenland sea. Geol. Soc. Am. Bull. 88, 969–999.
Terzaghi, R.D., 1965. Sources of error in joint surveys. Geotechnique 15, 287–304.
Tiab, D., Restrepo, D.P., Igbokoyi, A., 2006. Fracture porosity of naturally fractured reservoirs. SPE J. 104056, 13.
Uchman, A., Hanken, N.-M., Nielsen, J.K., Grundvåg, S.-A., Piasecki, S., 2016. Depositional environment, ichnological features and oxygenation of Permian to earliest Triassic marine sediments in central Spitsbergen, Svalbard. Polar Res. 35.
Van Stappen, J., Meftah, R., Boone, M., Bultreys, T., De Kock, T., Blykers, B., Senger, K., Olaussen, S., Cnudde, V., 2018. In-situ triaxial testing to determine fracture permeability and aperture distribution for CO2 sequestration in Svalbard, Norway. Environ. Sci. Technol. 52, 4546–4554.
Vaughan, A., Collins, N., Krus, M., Rourke, P., 2014. Recent Development of an Earth Science App-FieldMove Clino, EGU General Assembly Conference Abstracts.
Vöge, M., Lato, M.J., Diederichs, M.S., 2013. Automated rockmass discontinuity mapping from 3-dimensional surface data. Eng. Geol. 164, 155–162.
Watkins, H., Bond, C.E., Healy, D., Butler, R.W., 2015. Appraisal of fracture sampling methods and a new workflow to characterise heterogeneous fracture networks at outcrop. J. Struct. Geol. 72, 67–82.
Wennberg, O.P., Casini, G., Jonoud, S., Peacock, D.C., 2016. The Characteristics of Open Fractures in Carbonate Reservoirs and Their Impact on Fluid Flow: a Discussion.
Westoby, M., Brasington, J., Glasser, N., Hambrey, M., Reynolds, J., 2012. 'Structure-from-Motion'photogrammetry: a low-cost, effective tool for geoscience applications. Geomorphology 179, 300–314.
Wignall, P.B., Morante, R., Newton, R., 1998. The Permo-Triassic transition in Spitsbergen: $d^{13}C_{org}$ chemostratigraphy, Fe and S geochemistry, facies, fauna and trace fossils. Geol. Mag. 135, 47–62.
Witherspoon, P.A., Wang, J.S., Iwai, K., Gale, J.E., 1980. Validity of cubic law for fluid flow in a deformable rock fracture. Water Resour. Res. 16, 1016–1024.
Worsley, D., 2008. The post-Caledonian development of Svalbard and the western Barents Sea. Polar Res. 27, 298–317.
Worsley, D., Aga, O.J., Dalland, A., 1986. The Geological History of Svalbard: Evolution of an Arctic Archipelago. Den norske stats oljeselskap as.
Wuestefeld, P., De Medeiros, M., Koehrer, B., Sibbing, D., Kobbelt, L., Hilgers, C., 2016. Automated Workflow to Derive LIDAR Fracture Statistics for the DFN Modelling of a Tight Gas Sandstone Reservoir Analog, 78th EAGE Conference and Exhibition 2016. European Association of Geoscientists & Engineers, pp. 1–5.
Xu, S., Payne, M.A., 2009. Modeling elastic properties in carbonate rocks. Lead. Edge 28, 66–74.
Zeeb, C., Gomez-Rivas, E., Bons, P.D., Blum, P., 2013. Evaluation of sampling methods for fracture network characterization using outcrops. AAPG Bull. 97, 1545–1566.